Cosmic Microwave Background: cosmology from the Planck perspective

Gianfranco De Zotti[1]

1. INAF-Osservatorio Astronomico di Padova,
Vicolo dell'Osservatorio 5, I-35122 Padova, Italy

The *Planck* mission has measured the angular anisotropies in the temperature of the Cosmic Microwave Background (CMB) with an accuracy set by fundamental limits. These data have allowed the determination of the cosmological parameters with extraordinary precision. These lecture notes present an overview of the mission and of its cosmological results. After a short history of the project, the *Planck* instruments and their performances are introduced and compared with those of the WMAP satellite. Next the approach to data analysis adopted by the *Planck* collaboration is described. This includes the techniques for dealing with the contamination of the CMB signal by astrophysical foreground emissions and for determining cosmological parameters from the analysis of the CMB power spectrum. The power spectra measured by *Planck* were found to be very well described by the standard spatially flat six-parameter ΛCDM cosmology with a power-law spectrum of adiabatic scalar perturbations. This is a remarkable result, considering that the six parameters account for the about 2500 independent power spectrum values measured by *Planck* (the power was measured for about 2500 multipoles), not to mention the about one trillion science samples produced. A large grid of cosmological models was also explored, using a range of additional astrophysical data sets in addition to *Planck* and high-resolution CMB data from ground-based experiments. On the whole, the *Planck* analysis of the CMB power spectrum allowed to vary and determined 16 parameters. Many other interesting parameters were derived from them.

Although *Planck* was not initially designed to carry out high accuracy measurements of the CMB polarization anisotropies, its capabilities in this respect were significantly enhanced during its development. The quality of its polarization measurements have exceeded all original expectations. *Planck*'s polarisation data confirmed and improved the understanding of the details of the cosmological picture determined from its temperature data. Moreover, they have provided an accurate determination of the optical depth for Thomson scattering, τ, due to the cosmic reionization. The result for τ has provided key information on the end of "dark ages" and largely removed the tension with the constraints on the reionization history provided by optical/UV data, indicated by earlier estimates. This has dispensed from the need of exotic energy sources in addition to the ionizing power provided by massive stars during the early galaxy evolution. A joint analysis of BICEP2, Keck Array, and *Planck* data has shown that the B-mode polarization detected by the BICEP2 team can be accounted for by polarized Galactic dust and has tightened the constraint on the B-mode amplitude due to primordial tensor perturbations.

1 Introduction

A synthetic review of the theory and the observations on spectral distortions and on anisotropies of the Cosmic Microwave Background (CMB) was presented at the 1st Kielce Cosmology School. The lecture notes (De Zotti & Negrello, 2015) were published in the proceedings of the School. The lectures at the 2nd Kielce Cosmology School did not contain significant novelties on spectral distortions. Therefore this topic will not be further dealt with here.

In these notes I present an overview of the *Planck* mission (Section 2), a synthetic description of *Planck* instruments and of their performances, also compared to WMAP (Section 3). In Section 4 I briefly describe the techniques adopted for separating the various components present in the *Planck* maps. Next I update the previous review on temperature and polarization anisotropies, focussing on aspects that were touched upon only rapidly in the previous lecture notes (Sections 5 and 6). The basics of the theory of CMB anisotropies are recalled only in broad terms. For more details the reader is referred to De Zotti & Negrello (2015, and references therein) and to the slides of the lectures available in the School site[1].

2 The *Planck* mission

The history of the *Planck* mission begins in 1992, in the wake of the first detection of CMB temperature anisotropies on $\sim 10^\circ$ angular scales by the Differential Microwave Radiometers (DMR) experiment aboard the COsmic Background Explorer (COBE) (Smoot et al., 1992). This discovery triggered a flurry of ground-based and suborbital experiments aimed at mapping the CMB anisotropies down to much smaller scales.

It was clear, however, that only a space experiment could provide an accurate mapping on scales from a few arcminutes to the full sky with a thorough control of foreground emissions. These are the requirements to extract detailed information on the initial conditions that lead to the formation of the large scale structure of the universe, on the physics of the early universe and on its geometry and dynamics.

In November 1992 the European Space Agency (ESA) issued a call for new mission proposals for the third medium size mission (M3) of the Horizon 2000 scientific program. In May 1993, in response to this call, two proposals devoted to the study of CMB anisotropies were submitted: COBRAS (COsmic Background Radiation Anisotropy Satellite) and SAMBA (SAtellite for Measurement of Background Anisotropies). Both instruments were conceived as 1 meter class telescopes, each carrying broad-band detection systems fed by corrugated horns working at four different frequencies but with different technologies. COBRAS (P.I.: N. Mandolesi) used passively cooled radiometric receivers based on High Electron Mobility Transistors (HEMTs) low noise amplifiers, operating in the frequency range 30 to 130 GHz. SAMBA (P.I.: J.-L. Puget) used very low temperature bolometers operating in the range 140 to 800 GHz.

Recognizing the fundamental importance of the problem, further to the recommendation of the Astronomy Working Group (AWG), in September 1993 ESA's Space Science Advisory Committee (SSAC) recommended a full assessment study of a mission to investigate the CMB with scientists from both the COBRAS and SAMBA teams brought together with the aim of finding the most effective means for a European mission in this area.

[1] `http://www.cosmology-school.ujk.edu.pl/`

It was quickly recognized that a broad frequency coverage was required because of the need to accurately remove foreground sources of emission from the observed signal to obtain clean maps of the CMB. The removal is possible because the spectral shapes of foregrounds are different from that of the CMB. However the foreground components are numerous (zodiacal light, synchrotron, free-free and other kinds of dust emission from our Galaxy, extragalactic sources, Sunyaev-Zeldovich effect from galaxy clusters) and complex. This means that reliable foreground removal requires more frequency channels and a wider frequency range than it was possible to achieve, for technical reasons, by each of the proposed instruments, but could be achieved by merging the two instruments into one payload.

The two proposals were then used by an ESA-led team to design a payload where a single COBRAS-like telescope fed two instruments, a COBRAS-like Low Frequency Instrument (LFI), and a SAMBA-like High Frequency Instrument (HFI) sharing a common focal plane. The assessment study, carried out between December 1993 and May 1994, showed that the combined COBRAS/SAMBA mission could survey most of the sky with an angular resolution better than $0^\circ.2$, a sensitivity better than $\Delta T/T \sim 2 \times 10^{-6}$ and covering a frequency range wide enough to enable a reliable separation of foreground emissions. In addition to the primary objective (mapping of CMB anisotropies) the satellite would provide unique data on a huge variety of astrophysical phenomena.

A phase A study of COBRAS/SAMBA was carried out between December 1994 and December 1995. The results of this study, reported by Bersanelli et al. (1996), confirmed and enhanced the scientific case for COBRAS/SAMBA elaborated during the assessment study. Detailed design options for the payload instruments and the telescope were developed and it was proven that the mission could be carried out within the technical and financial constraints of the M3 call for proposals.

In July 1996 ESA's Science Program Committee (SPC) selected COBRAS/SAMBA as the M3 mission. The launch was foreseen in 2004-2005. Shortly after the mission was approved, it was renamed in honor of the German scientist Max Planck (1858–1947), winner of the Nobel Prize for Physics in 1918.

ESA released an Announcement of Opportunity for *Planck* instruments in October 1997. In November 1997 the SPC endorsed a revised baseline scenario of Horizons 2000, presented by the Executive, which assumed a launch date delayed to mid-2006. The proposals for the LFI and the HFI instruments, presented in February 1998, were both formally accepted in February 1999, after a detailed review by independent scientists. The telescope mirrors were provided by ESA and a consortium of Danish institutes (DK-Planck) led by H.U. Noorgard-Nielsen. Each of the three consortia (LFI, HFI and DK-Planck) had the responsibility to design, procure and deliver to ESA their hardware. The LFI and HFI consortia had the additional responsibility to operate their respective instrument and to set up Data Processing Centers (DPCs) to process all the scientific data into usable scientific products. ESA was responsible for the spacecraft, integration of instruments and spacecraft, launch, mission operations and distribution of the scientific products to the larger scientific community.

Shortly after its selection, the development of *Planck* was joined with that of ESA's *Herschel* Space Telescope (called FIRST at the time), based on a number of potential commonalities, the most important of which was that both missions targeted orbits around the second Lagrangian point (L2) of the Sun-Earth-Moon system. Thus the two satellites could share a single heavy launcher.

L2 is located 1.5 million kilometres directly 'behind' the Earth as viewed from the

Sun. It is about four times further away from the Earth than the Moon ever gets and orbits the Sun at the same rate as the Earth. The orbit described a Lissajous trajectory around L2 with a ~ 6 month period. The required lifetime of *Planck* in routine operations (i.e., excluding transfer to orbit, commissioning and performance verification phases which span ~ 3 months in total) was 15 months, allowing it to complete two full surveys of the sky (*Planck* nominal mission). Its total lifetime was limited by the active coolers required to operate its detectors. In particular:

- the dilution cooler, which cools the *Planck* bolometers to 0.1 K, uses ^{3}He and ^{4}He gas, stored in tanks and vented to space after the dilution process. Pre-launch tests have verified that the tanks carried enough gas to provide an additional lifetime of between 11 and 15 months over the nominal lifetime, depending on the exact operating conditions in flight.

- the lifetime of the hydrogen sorption refrigerator, which cools the radiometers to 20 K and provides a first pre-cooling stage for the bolometer system, is limited by gradual degradation of the sorbent material. Two units flew on *Planck*. It was expected that the first allowed completion of the nominal mission and the second allowed an additional 14 months of operation. A further increase of lifetime could be obtained by a process known as "regeneration".

The *Planck* spacecraft rotated about a Sun-pointed axis. Its geometrical configuration was designed to prevent stray light originating from the Sun, the Earth and the Moon from reaching the focal plane and to allow the greatest possible thermal isolation of the warm spacecraft from the cold payload. The *Planck* orbit subtended a maximum angle of 15°, as seen from the Earth. In this way *Planck* could always maintain its payload pointed towards deep space, shielded from solar, Earth and lunar illumination by its solar array.

A series of financial and development problems caused delays in the launch date that was successively postponed to February 2007, then to February 2008 and finally to 2009. *Herschel* and *Planck* were launched on an Ariane 5 rocket on 14th May 2009 from Kourou, French Guiana. Within 30 minutes after launch the two satellites were separated from the rocket and proceeded independently to their respective orbits, using autonomous hydrazine-based propulsion systems. *Planck* arrived at L2 on July 3rd, about six weeks after launch, following a few trajectory correction manoeuvres, and entered its operational orbit. Its payload and all the spacecraft subsystems were found to work at nominal temperatures.

The first all sky survey started on August 13, 2009, after the successful conclusion of the commissioning phase. On January 15th, 2010 ESA approved an extension of *Planck* operations by 12 months. The nominal mission ended on November 26, 2010; at this time *Planck* was planned to continue surveying the sky until the exhaustion of its cryogenic consumables. The HFI ran out of coolant on January 14, 2012 as expected, after having almost completed the fifth survey of the sky. The LFI operations were extended by 12 months and then by further 6 months, allowing the instrument to complete a total of 8 sky surveys. On October 4, 2013 the routine operations were ended and the decommissioning activities started. At the end of its mission *Planck* was put into a heliocentric orbit and passivated to prevent it from endangering any future missions. The final command to the *Planck* satellite was sent on 23 October 2013, marking the end of operations.

The first delivery to the public of *Planck* data was the Early Release Compact Source Catalogue (ERCSC), released on 11 January 2011 together with a set of 25

scientific papers. On August 10, 2015, the full *Planck* data were delivered to the *Planck* Legacy Archive (PLA; `http://pla.esac.esa.int/pla/#home`) which hosts the mission products. The PLA comprises a full record of the data and results from the mission. This includes: all-sky maps of intensity at all of the nine Planck frequency channels, with all-sky polarisation maps for seven of the frequencies; all-sky CMB temperature maps; maps detailing different foreground emissions, extensive catalogues of compact sources, Sunyaev-Zeldovich detections and Galactic cold clumps; and much more.

The PLA is open for exploitation by the scientific community. There is no doubt that a lot of important information in many fields of astronomy, not dealt with in papers by the *Planck* collaboration, can be gleaned from it. Although the archive is now complete in terms of data products, the *Planck* collaboration is continuing to improve the data calibration and a new release is expected in late 2016 or early 2017.

3 The *Planck* instruments

As mentioned above, *Planck* carried 2 instruments, the Low Frequency Instrument (LFI; Principal Investigator: N. Mandolesi) and the High Frequency Instrument (HFI; P.I.: J.-L. Puget).

The LFI is described in Bersanelli et al. (2010) and Mennella et al. (2010). It comprises 11 radiometer chain assemblies (RCAs), two at 30 GHz, three at 44 GHz, and six at 70 GHz, each composed of two independent pseudo-correlation radiometers sensitive to orthogonal linear polarization modes. The original LFI proposal also anticipated a 100 GHz channel with 34 polarised detectors. This would have yielded an overlap in frequency with the HFI. The comparison of data at the same frequency obtained with independent technologies would have made possible an excellent cross-check and control of instrument-specific systematic effects. Unfortunately the 100 GHz LFI channel could not be funded by the Italian Space Agency (ASI).

Each radiometer has two independent square-law diodes for detection, integration, and conversion from radio frequency signals to DC voltages. The focal plane was cryogenically cooled to 20 K, while the pseudo-correlation design uses internal, black-body reference loads cooled to 4.5 K. The radiometer timelines are produced by taking differences between the signals from the sky, V_{sky}, and from the reference loads, V_{ref}.

A summary of the instrument performance parameters measured in flight during the four years of operation of LFI is given in Table 1 (Planck Collaboration II, 2016). Optical properties, the Full Widths at Half Maximum (FWHMs) and the beam ellipticities during the scans, were reconstructed by fitting Jupiter observations directly in the timelines. The effective beam FWHMs take into account the specific scanning strategy and the pointing information in order to include any smearing and orientation effects on the beams themselves. They were used in the source extraction pipeline to determine the source photometry. The white noise level in timelines given in Table 1 are typical values derived from fitting the noise spectra.

The data in the following rows of the Table are from Planck Collaboration I (2016). The end-of-mission temperature and polarisation noises are computed after smoothing to 1° resolution to have a homogeneous comparison among channels with different resolutions. The overall calibration uncertainty is the sum of the errors determined from the absolute and relative calibration. The systematic effects uncertainties are estimated root mean square (rms) values over the full sky and after the full mission integration.

Table 1: LFI performance parameters.

Frequency	30	44	70
Number of detectors	4	6	12
Scanning beam FWHM [arcmin]	33.10	27.94	13.08
Scanning beam ellipticity	1.37	1.25	1.27
Effective solid solid angle $\Omega_{\rm eff}$ [arcmin^2]	1190	832	201
Effective beam FWHM [arcmin]	32.29	27.00	13.21
White noise level in timelines [$\mu{\rm K_{CMB}\,s^{1/2}}$]	148.1	174.2	152.0
End-of-mission temperature noise [$\mu{\rm K_{CMB}\,deg}$]	2.5	2.7	3.5
End-of-mission polarisation noise [$\mu{\rm K_{CMB}\,deg}$]	3.5	4.0	5.0
Overall calibration uncertainty [%]	0.35	0.26	0.20
Systematic effects uncertainty in Stokes I [$\mu{\rm K_{CMB}}$]	0.19	0.39	0.40
Systematic effects uncertainty in Stokes Q [$\mu{\rm K_{CMB}}$]	0.20	0.23	0.45
Systematic effects uncertainty in Stokes U [$\mu{\rm K_{CMB}}$]	0.40	0.45	.44

Table 2: HFI performance parameters.

Frequency (GHz)	100	143	217	353	545	853
Number of bolometers	8P	8P+4	8P+4	8P+4	4	4
Effective beam FWHM [arcmin]	9.68	7.30	5.02	4.94	4.83	4.64
Effective beam ellipticity	1.186	1.040	1.169	1.166	1.137	1.336
Effective solid solid angle $\Omega_{\rm eff}$ [arcmin^2]	102.22	60.44	28.57	27.69	26.44	24.37
White noise level [$\mu{\rm K_{CMB}\,s^{1/2}}$]	41.3	17.4	23.8	78.8	...	...
White noise level [$\rm kJy\,s^{1/2}$]	...	...	...	...	24.0	22.2
EoM temperature noise [$\mu{\rm K_{CMB}\,deg}$]	1.29	0.55	0.78	2.56	...	...
EoM intensity noise [$\rm kJy\,sr^{-1}\,deg$]	...	...	...	...	0.78	0.72
EoM polarisation noise [$\mu{\rm K_{CMB}\,deg}$]	1.96	1.17	1.75	7.31	...	...
Calibration uncertainty [%]	0.09	0.07	0.16	0.78	1.1 (+5)	1.4 (+5)

Table 3: WMAP performance parameters.

Band	K	Ka	Q	V	W
Effective frequency (GHz)	22.8	33.0	40.7	60.8	93.5
Number of detectors	4	4	8	8	16
Effective solid solid angle $\Omega_{\rm eff}$ [arcmin^2]	2981	1731	1074	503	247
FWHM$_{\rm eff}$ [arcmin]	49.2	37.2	29.4	19.8	12.6
Sensitivity [$\mu{\rm K_{CMB}\,s^{1/2}}$]	659	802	960	1241	1842
End-of-mission temperature noise [$\mu{\rm K_{CMB}\,deg}$]	41	41	39	47	56
End-of-mission polarisation noise [$\mu{\rm K_{CMB}\,deg}$]	57	57	54	66	79

The HFI (Lamarre et al., 2010; Planck HFI Core Team, 2011) used cold optics and 52 bolometers cooled to 100 mK to map the continuum emission of the sky in six bands, centered at 100, 143, 217, 353, 545 and 857 GHz, with a sensitivity limited by the photon noise of the observed radiation. The four lower frequency bands (100 to 353 GHz) were dedicated to direct measurement of the CMB and were polarisation sensitive. The two highest frequency bands were optimised to identify the foregrounds (mostly Galactic dust emission, extragalactic sources and zodiacal light) and to separate them from the CMB. They only measured radiation intensity, not polarisation. The low frequency limit of the HFI spectral coverage was set mainly by the bolometer technology that, at the time, was not developed at longer wavelengths. A combination of radiative cooling and three mechanical coolers provided the temperatures needed for the detectors and optics to reach the required sensitivity.

The HFI performance parameters measured in flight are summarized in Table 2. The data are from Planck HFI Core Team (2011) and Planck Collaboration VIII (2016). In the second row the "P" identifies the polarisation sensitive bolometers (at 100 GHz all bolometers are polarisation sensitive; at 143, 217 and 353 GHz 8 over 12 are polarisation sensitive; polarisation is not measured at higher frequencies). The FWHM is that of a Gaussian whose solid angle is equivalent to that of the effective beam. The effective beam ellipticity is the ratio of the major to minor axis of the best elliptical Gaussian fit averaged over the full sky. As in the LFI case, the end-of-mission (EoM) temperature and polarisation noises are computed after smoothing to 1° resolution.

Two different photometric calibration schemes have been used for HFI. The 545 and 857 GHz data were calibrated in surface brightness (MJy/sr) using Uranus and Neptune as calibration sources. In the latest HFI data processing (Planck Collaboration VIII, 2016) the lower frequencies (from 100 to 353 GHz) were calibrated in thermodynamic temperature (K_{CMB}) using the *orbital* dipole.

The anisotropy induced by the motion of the instrument relative to the cosmological frame is naturally separated into two components. The component generated by the motion of *Planck* around the Sun was called the *orbital* dipole while that generated by the Sun's motion relative to the CMB was called the *solar* dipole. The orbital dipole is the most precise calibrator, as it depends on the very well known orbital parameters and on the temperature of the CMB, measured precisely by the COBE/FIRAS experiment (Fixsen & Mather, 2002). It was therefore preferred to the solar dipole used for the previous HFI photometric calibration (Planck Collaboration VIII, 2014). At high frequency ($\nu > 500$ GHz), the dipole becomes too faint with respect to the Galactic foregrounds to give an accurate calibration; better accuracy was achieved using planet measurements. In the last line of Table 2, at 545 and 857 GHz the 5% accounts for the uncertainty in the model atmospheres of Uranus and Neptune.

While the *Planck* mission was being developed, the NASA launched and operated the Microwave Anisotropy Probe (MAP; P.I.: C.L. Bennett) which, in 2003, was renamed WMAP in honor of the cosmologist D. T. Wilkinson (1935–2002) who had been a member of the mission's science team. The MAP mission was proposed to NASA in 1995, selected for definition study in 1996, and approved for development in 1997, i.e. after the selection of COBRAS/SAMBA as ESA's M3 mission. It was launched via a Delta II 7425 rocket on June 30, 2001 and arrived to L2 on October 1, 2001. The nominal science operations ended on 10 August 2010 (Greason et al., 2012).

The much shorter timescale of WMAP compared to *Planck* reflects on one side the different approaches of ESA and NASA to space missions and on the other side the more advanced, challenging and complex *Planck* technology. Table 3 shows some WMAP performance parameters. The effective frequencies of its 5 frequency bands are slightly dependent on the spectrum of the source (the same is obviously true also for *Planck*); the values given in Table 3, taken from Page et al. (2003), refer to the CMB spectrum. To have a feeling of the dependence on the source spectra the reader may have a look at Table 3 of Bennett et al. (2013) which gives the effective center frequencies for a point source with flux density spectral index $\alpha = -0.1$ ($S_\nu \propto S^\alpha$); the difference ranges from $\lesssim 0.1$ GHz to $\simeq 0.5$ GHz.

The effective solid angles, taken from Bennett et al. (2013), are for point sources with flux density spectral index $\alpha = -0.1$. Since the WMAP beams are not Gaussian, the listed values of the effective FWHMs, taken from Table 5 of Page et al. (2003), are purely illustrative and meant to ease the comparison with the *Planck* resolution. The sensitivity is given in Table 1.3 of Greason et al. (2012) in antenna (Rayleigh-Jeans) temperature, δT_A. For a direct comparison with the corresponding *Planck* values (white noise level in timelines) I've converted δT_A into variations of the thermodynamic (CMB) temperature, δT_CMB in $\mu\mathrm{K_{CMB}}$ using the formula:

$$\delta T_\mathrm{CMB} = \frac{(e^x - 1)^2}{x^2 e^x} \delta T_\mathrm{A}, \tag{1}$$

where $x = h\nu_\mathrm{eff}/kT_\mathrm{CMB} \simeq 1.761(\nu_\mathrm{eff}/100\,\mathrm{GHz})$, h and k being the Planck and Boltzmann constants, respectively, and $T_\mathrm{CMB} = 2.725$ K (Fixsen & Mather, 2002).

The end-of-mission typical temperature and polarisation noise values, smoothed to 1° resolution, for WMAP are my own estimates based on the information in (Greason et al., 2012). A comparison of the sensitivities and angular resolutions listed in Tables 3, 1 and 2 illustrates the substantial improvement of *Planck* over WMAP.

4 Component separation

Another great advantage of *Planck* over WMAP is its much broader spectral coverage that allowed a better control of foreground emissions in both temperature and polarization, and actually to construct separate maps of each emission component. However, the 9-yr WMAP observations were also incorporated in the analysis to get a coherent astrophysical model of the microwave sky in temperature (Planck Collaboration X, 2016).

The foregrounds are divided into two distinct categories: diffuse emission from the Milky Way (the Galaxy) and compact sources. The Galactic foregrounds are the main contaminant of the CMB maps on large angular scales. The power spectrum of their fluctuations decreases roughly as a power law with increasing multipole number (Planck Collaboration XII, 2014; Planck Collaboration XV, 2014). They are dominated by synchrotron, free-free (bremsstrahlung) and anomalous microwave emission (AME, ascribed to spinning dust grains, a new foreground component not foreseen at the time of the planning of the *Planck* mission) at frequencies below 70 GHz, and by thermal dust emission and rotational line emission from carbon monoxide (CO) molecules at frequencies above 100 GHz (another component not foreseen).

Extragalactic foregrounds, on the other hand, dominate the small-scale contamination of the CMB. They arise from discrete radio and far-infrared sources, primarily dusty galaxies, and also from the Sunyaev-Zeldovich (SZ) effect (Sunyaev & Zeldovich, 1972) in galaxy clusters. The brightest ones are individually detected (Planck

Collaboration XXVI, 2016; Planck Collaboration XXVII, 2016) and can therefore be masked or subtracted out. Fainter sources produce small scale fluctuations due to their inhomogeneous distribution. Such fluctuations have two contributions, due to shot (Poisson) noise and to clustering, respectively (De Zotti et al., 2015). The latter contribution is generally negligible in the case of radio sources and of the SZ effect but is dominant on the *Planck* angular scales in the case of dusty galaxies.

In the *Planck* analyses, foregrounds are dealt with in a variety of ways. At the power spectrum and likelihood level, the extragalactic foregrounds are modelled with parameterized power spectra, appropriate to their statistical isotropy, over regions restricted to low Galactic emission (Planck Collaboration XV, 2014).

The four methods used by *Planck* to separate the CMB from diffuse foreground emission are described in detail in Planck Collaboration XII (2014). They were selected out of a set of eight methods that were developed and assessed within the *Planck* "Component Separation Working Group" (WG2) activity using realistic simulations of the sky in temperature and polarisation (Leach et al., 2008).

The selected methods are representative of the main approaches to component separation developed in recent years. They can be divided into two types. The first type assumes only knowledge of the black-body spectrum of the CMB, and the foregrounds are removed by combining the multi-frequency data to minimize the variance of the CMB component. The second type constructs an explicit parameterized model of the CMB and foregrounds with an associated likelihood. The CMB component is obtained by maximizing or sampling from the posterior distribution of the parameters. Both types may be implemented in the map domain or in the harmonic domain. A brief description of their main features follows.

Commander (Eriksen et al., 2006, 2008) is a Bayesian parametric method that works in the map domain. Both the CMB and the foregrounds are modelled using a physical parametrization in terms of amplitudes and frequency spectra. The joint solution for all components is obtained by sampling from the posterior distribution of the parameters given the likelihood and a set of priors. To produce a high-resolution CMB map, the separation is performed at multiple resolutions with different combinations of input channels. The final CMB map is obtained by combining these solutions in the spherical harmonic domain. A low-resolution version of the separation is used to construct the CMB temperature power spectrum likelihood for large angular scales (Planck Collaboration XI, 2016). Commander employs detector and detector set maps rather than full frequency maps, and excludes some specific detector maps judged to have significant systematic errors. Thus, the selection of data is not identical between Commander and the other three methods.

NILC (Delabrouille et al., 2009) is an implementation of internal linear combination (ILC) that works in the needlet (wavelet) domain. The ILC component separation method considers one of the components (the CMB) to be the only emission of interest, all the other being unwanted contaminants. It is assumed that the spatial distribution of the component of interest is the same at all frequencies of observation, and that the observations are calibrated with respect to this component. The input maps are decomposed into needlets at a number of different angular scales. The solution for the CMB is produced by minimizing the variance at each scale. This has the advantage that the weights used to combine the data can vary with position on the sky and also with angular scale. The solutions are then combined to produce the final CMB map.

SEVEM (Spectral Estimation Via Expectation Maximisation; Martínez-González et al., 2003; Fernández-Cobos et al., 2012) is an implementation of the template-cleaning approach to component separation that works in the map domain. It does not need a thorough knowledge of foregrounds because it obtains all the information to construct different templates from the data. Foreground templates are constructed by differencing pairs of maps from the low- and high-frequency channels. The differencing removes the CMB contribution to the templates that are then used to clean each CMB-dominated frequency channel by finding a set of coefficients that minimize the variance of the map outside of a mask. Thus SEVEM produces multiple foreground-cleaned frequency channel maps. The final CMB map is produced by combining a number of the cleaned maps in harmonic space.

SMICA (Spectral Matching Independent Component Analysis; Cardoso et al., 2008) is a non-parametric method that works in the spherical harmonic domain. The Independent Component Analysis (ICA) is an approach to the "blind component separation" that exploits a fascinating possibility: if the components of a linear mixture are statistically independent, they can be recovered even if the mixing matrix[2] $\mathbf{A}$ is unknown a priori. In the SMICA application, foregrounds are modelled as a small number of templates with arbitrary frequency spectra, arbitrary power spectra, and arbitrary correlation between the components. The solution is obtained by minimizing the mismatch of the model to the auto- and cross-power spectra of the frequency channel maps. From the solution, a set of weights is derived to combine the frequency maps in the spherical harmonic domain to produce the final CMB map. Maps of the total foreground emission in each frequency channel can also be produced. In the analysis performed for the 2013 release (Planck Collaboration XII, 2014), SMICA was the method that performed best on the simulated temperature data

The above methods, initially applied to *Planck* temperature data (Planck Collaboration XII, 2014), were extended to operate on polarization data in Planck Collaboration IX (2016). A key distinction between the methods is the choice of operating domain. Two of the methods, Commander and SEVEM, operate in the map domain, so it is most natural for them to perform the polarized component separation on the Q and U maps. The other two methods, NILC and SMICA, operate in the harmonic or needlet domain. An intrinsic part of the transform of polarized maps to these domains is the decomposition of Q and U into E- and B-modes (see Sect. 6), which is accomplished by using spherical harmonic transforms on the full sky. Thus these two methods perform their separation directly on E and B.

The foreground sky turned out to be more complex than expected before *Planck* observations. In addition to the well known diffuse components (zodiacal light, synchrotron, free-free and thermal dust), *Planck* has unambiguously detected a new Galactic emission component spatially correlated with thermal dust, called Anomalous Microwave Emission (AME). Its spectrum, generally peaks at 20–30 GHz (but there are regions with a peak shifted to higher frequencies; Planck Collaboration XXV, 2016) and rapidly declines at higher and lower frequencies. This shape is compatible with the model of Draine & Lazarian (1998) which attributes this emission to small spinning dust particles. Evidences of this component were found in a variety of data sets but its interpretation was controversial (de Oliveira-Costa et al., 2004). The WMAP team challenged this interpretation (Bennett et al., 2003), arguing that

[2]Let y be the vector containing the observations at the different frequencies which are a mixture of the signals s from the various components. Then can write the observations as $y = \mathbf{A}s$.

the foreground emission observed at the five WMAP frequencies could be entirely accounted by only three foreground emission components (synchrotron, free-free and thermal dust) with no solid evidence for the AME. But a detailed analysis of the WMAP data by Davies et al. (2006) revealed the presence in selected areas of an additional component with AME properties. Later analyses have made the association of the AME with spinning dust much firmer (Planck Collaboration XX, 2011; Planck Collaboration XXI, 2011; Bennett et al., 2013; Planck Collaboration Int. XV, 2014). *Planck* reached up to provide all sky maps of all diffuse components, including the AME (Planck Collaboration X, 2016).

Moreover, molecular lines turned out to have a larger impact on *Planck* maps than was foreseen before launch. The first nine rotational transition lines from carbon monoxide (CO) lie within the spectral bands of the HFI instrument. Of these, the first three, $J = 1 \rightarrow 0$, $J = 2 \rightarrow 1$, and $J = 3 \rightarrow 2$ at 115.271, 230.538 and 345.796 GHz, respectively, present the largest transmission coefficients making them a significant component of the intensity maps in *Planck* 100, 217, and 353 GHz frequency channels. The $J = 4 \rightarrow 3$ and $J = 5 \rightarrow 4$ transitions at 461.041 and 576.268 GHz, respectively, which are within the 545 GHz band, and the $J = 6 \rightarrow 5$, $J = 7 \rightarrow 6$, $J = 8 \rightarrow 7$ and $J = 9 \rightarrow 8$ transitions at 691.473, 806.652, 921.799, 1036.912 GHz, which are within the 857 GHz band, did not give a detectable signal.

Three methods were used to build all-sky maps of the first three CO lines:

- the single-channel approach exploits differences in the spectral band-passes of the bolometers within a frequency channel, resulting in differences of the spectral transmission of a given CO line so that the fraction of CO emission with respect to the total emission is also different;
- the multi-channel approach makes use of the intensity maps in several channels to isolate the CO contribution from other astrophysical sources of emission, exploiting the fact that the emissions mentioned above vary smoothly from channel to channel, while the CO emission does not (for example it is totally absent in the 70 and 143 GHz channels but is relatively strong in the 100 GHz channel);
- the multi-line approach assumes that the line ratios $CO(2 \rightarrow 1)/CO(1 \rightarrow 0)$ and $CO(3 \rightarrow 2)/CO(1 \rightarrow 0)$ are constant across the sky. The sky is modelled as a superposition of CMB, CO, dust (treated as a grey-body) and a power law to describe the low frequency Galactic emission; a single CO map is solved for.

The CO maps obtained with the three methods are called Type 1, Type 2 and Type 3, respectively. Type 3 maps were delivered only with the 2013 data release, not with the 2015 one.

The 2015 *Planck* data release includes also a new general line emission map, which captures a combination of emission lines that are contributing to the measured signal in the HFI 100 GHz and in the WMAP W (94 GHz) bands (Planck Collaboration X, 2016). An important contributor to this map is the HCN line at 88.6 GHz, providing about 23% of the 100 GHz amplitude and about 63% of the W-band amplitude towards the Galactic circumnuclear disk and Sgr A$*$. Several other lines (CN, $HCO+$, CS, etc.) contribute at a level of 5–10% each and there is also a non-negligible, but not easily quantifiable, amount of CO leakage in this new map that is therefore referred to as "94/100 GHz line emission".

Of course, in addition to the zodiacal light and to the Galactic emission components mentioned above, the *Planck* maps contain extragalactic sources: radio sources,

dusty galaxies making up the Cosmic Infrared Background (CIB), the thermal SZ effect and the weaker kinetic SZ effect in clusters of galaxies. With the exceptions of the SZ effects and, to a good approximation, of the free-free, all these components have spatially varying spectra.

It is thus clear that *Planck* had not enough frequency channels to solve for all components and had to include in the analysis other data sets like the 9-yr WMAP maps and the 408 MHz map (basically of Galactic synchrotron) by Haslam et al. (1982). It follows that the next generation CMB experiments need to use many more bands than *Planck*. In principle we have to deal with between 10 and 20 different physical components for a proper model in total intensity (depending on the level of detail required) and of course to solve for all of them we need a number of frequency channels at least equal to the number of components.

The situation is simpler for polarization. At the sensitivity level of current experiments, only three diffuse components have been clearly detected, namely CMB, synchrotron, and thermal dust. But at higher sensitivity other components may come in. The spinning dust emission is generated by small dust grains, and these generally align weakly with the local magnetic field. However, rotational energy level splitting dissipates energy, and this leads to a low level of grain alignment (Lazarian & Draine, 2000). As a result, the polarization fraction may be up to 1–3% between 10 and 30 GHz, but falling to less than 1% at higher frequencies. Upper limits at these levels have been obtained by the Q-U-I JOint TEnerife (QUIJOTE) intensity and polarisation measurements.

Polarized *CO* emission was detected by Greaves et al. (1999) at the roughly 1% level near the Galactic centre and in molecular clouds. The free-free emission process is intrinsically independent of direction, and therefore naturally unpolarized, although some polarization may arise due to Thomson scattering on electrons near the edges of strong HII regions. This effect, however, is smaller than 10% for the edges of optically thick clouds (Keating et al., 1998) and negligible away from any sharp edges. Averaged over the full sky, the free-free emission is observationally constrained to be less than a few percent (Macellari et al., 2011).

A small but significant contribution to polarisation on small scales comes from extragalactic radio sources, while the contribution of dusty galaxies is expected to be much smaller (De Zotti et al., 1999; Tucci & Toffolatti, 2012). Various mechanisms produce low polarisation levels of the SZ effect in galaxy clusters: the CMB quadrupole, cluster transverse motion, finite optical depth (Zeldovich & Sunyaev, 1980; Sazonov & Sunyaev, 1999). Although the signal is very weak, its detection would provide important information.

5 CMB temperature anisotropies

As mentioned in the Introduction, I will only briefly recall here the basics of CMB temperature anisotropies. More details can be found in the slides of the lectures and in De Zotti & Negrello (2015) and references therein.

5.1 The CMB power spectrum

The component separation methods were successful in producing a remarkably clean CMB map (see, e.g., Fig. 7 of Planck Collaboration X, 2016). However, some foreground residuals are unavoidable, especially in the Galactic plane region. Therefore,

temperature and polarization masks are used to discard areas of the sky that are seriously contaminated by foreground emission. The choice of masks is a trade-off between maximizing the sky coverage to minimize sample variance, and the complexity and potentially insufficient accuracy of the foreground model needed in order to deal with regions of stronger foreground emission.

Different masks, tailored for specific studies, were used for different *Planck* papers; they are described in the Appendix A of Planck Collaboration XI (2016) and in the Appendices A–D of Planck Collaboration IX (2016). In temperature, they combine a Galactic mask, excluding mostly low Galactic-latitude regions, and a point-source mask. As mentioned above, some components, including point sources at HFI frequencies, are irrelevant in polarisation and therefore masks are different. The masks can be freely accessed via the *Planck* Legacy Archive interface, like the other *Planck* products.

The map gives us the CMB intensity (or, equivalently, the CMB temperature) as a function of the direction on the sky. After removing the monopole (mean intensity) we are left with the temperature fluctuation map. It is convenient to expand it in spherical harmonics, $Y_{lm}(\theta,\phi)$, equivalent, on a spherical surface, to the Fourier expansion on the plane:

$$\Delta T(\theta,\phi) = \sum_{1}^{\infty} \sum_{m=-\ell}^{\ell} a_{\ell m} Y_{\ell m}(\theta,\phi). \tag{2}$$

Although the sum runs over $\ell \geq 1$, the dipole ($\ell = 1$) is usually subtracted since it is of local origin. Then, provided one goes to sufficiently high multipoles, and ignoring effects of beams and masking, one can use the set of $a_{\ell m}$'s as an alternative representation of the pixels in the map.

The power spectrum C_ℓ is the expectation value of the variance of the $a_{\ell m}$ as a function of ℓ, with each m being equivalent since there are no cosmologically preferred directions, as well as no dependence on spatial position (homogeneity):

$$\langle a^*_{\ell' m'} a_{\ell m} \rangle = C_\ell \delta_{\ell\ell'} \delta_{mm'}, \quad C_\ell = \langle |a_{\ell m}|^2 \rangle = \frac{1}{2\ell+1} \sum_m |a_{\ell m}|^2. \tag{3}$$

Angle brackets denote an average over many realizations and the $*$ denotes the complex conjugate. The first of the two equations (3) tells us that the a_{lm}'s are uncorrelated for different values of ℓ and m. If the fluctuations are also Gaussian, as predicted by the simplest inflationary models, all higher order statistics vanish so that

- the power spectrum provides a complete statistical description of anisotropies,
- the a_{lm}'s, hence the C_ℓ's are independent (remember that 'uncorrelated' is not equivalent to 'independent').

The mean square temperature fluctuation over an instrumental solid angle $\omega = 2\pi\theta^2$ is

$$\langle (\Delta T(\theta))^2 \rangle = \omega^2 \sum_\ell \frac{2\ell+1}{4\pi} W_\ell C_\ell \simeq \omega^2 \int \frac{\ell^2}{2\pi} C_\ell W_\ell d\ln\ell, \tag{4}$$

where W_ℓ is the window function describing the ℓ-space region observable with the considered instrument. For a Gaussian instrument beam with FWHM $= 2\sqrt{2\ln 2}\,\sigma_b$, $W_\ell = \exp(-\ell^2\sigma_b^2)$. Thus the quantity

$$D_\ell = \frac{\ell(\ell+1)}{2\pi} C_\ell \tag{5}$$

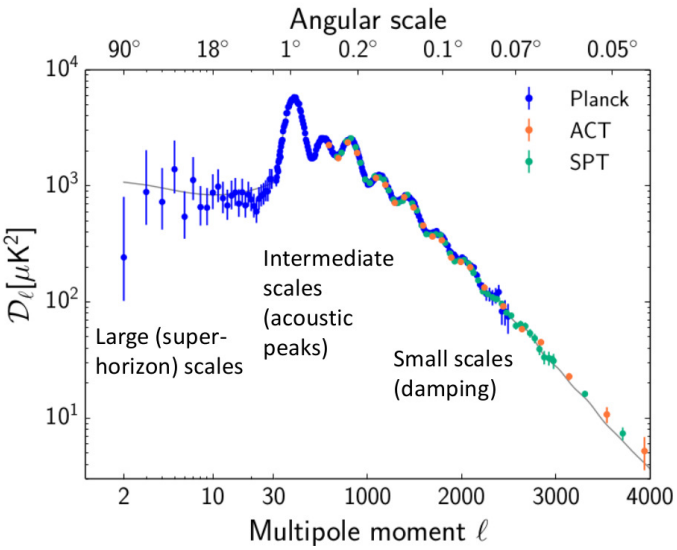

Fig. 1: The three regimes of the CMB temperature power spectrum. Adapted from Planck Collaboration XI (2016).

is approximately the power of temperature anisotropies per $\Delta \ln \ell = 1$. D_ℓ is the quantity that is frequently plotted instead of C_ℓ.

5.2 The sound horizon

As illustrated by Fig. 1, we can distinguish three regimes in the anisotropy power spectrum, corresponding to three critical scales, all defined at recombination: the sound horizon, the width of the last scattering shell and the damping scale. The *comoving* size of the sound horizon at recombination is the distance the sound could travel from $t = 0$ to recombination

$$r_s(t_{\rm rec}) = \int_0^{t_{\rm rec}} (1+z) c_s \, dt = \int_{z_{\rm rec}}^{\infty} c_s \, (1+z) \frac{dt}{dz} dz. \tag{6}$$

With accurate measurement of seven acoustic peaks, *Planck* has determined the observed angular size $\theta_* = r_s(z_*)/D_A(z_*)$ of the sound horizon at the decoupling redshift $z_\star$ to better than 0.1% precision (Planck Collaboration XIII, 2016, column: TT, TE, EE + lowP + lensing + ext of their Table 4):

$$\theta_* = (1.04112 \pm 0.00029) \times 10^{-2} \, {\rm rad} = 0.596518^\circ \pm 0.00017^\circ. \tag{7}$$

Since this parameter is constrained by the positions of the peaks but not by their amplitudes, it is quite robust. With the best fit values of the parameters, θ_* corresponds to a *comoving* linear size $r_s(z_*) = 144.81\,{\rm Mpc}$; the angular size distance is $D_A(z_*) = 13.909\,{\rm Gpc}$.

The effect of curvature and dark energy is negligibly small in the early universe, before recombination. The integral in eq. (6) can then evaluated analytically. Let's define $H_0 = h\,100\,{\rm km/s\,Mpc} = h/2.997.92\,{\rm Mpc}$, $\omega_m = h^2\Omega_m$, $\omega_b = h^2\Omega_b$, $\omega_r = h^2\Omega_r$ and $\omega_\gamma = h^2\Omega_\gamma$, where Ω_m, Ω_b and Ω_γ are the matter, baryon and photon energy densities in units of the critical density, and $\Omega_r = [1 + (7/8)N_\nu(4/11)^{4/3}]\Omega_\gamma$ is the

radiation energy density, including the contribution of N_ν neutrino species, assumed to be relativistic. Then we get[3]

$$r_s(t_*) = \frac{2.997.92\,\mathrm{Mpc}}{\sqrt{1+z_*}}\,\frac{2}{\sqrt{3\omega_m R_*}}\,\ln\frac{\sqrt{1+R_*}+\sqrt{R_*+r_*R_*}}{1+\sqrt{r_*R_*}} \tag{8}$$

where $r_* = \omega_r\,(1+z_*)/\omega_m$, $R_* = 3\omega_b/4\omega_\gamma\,(1+z_*)$. Thus the sound horizon depends on the two cosmological parameters ω_m and ω_b, plus a weak dependence on N_ν via ω_r (Ω_γ is known with high accuracy). Increasing either ω_m or ω_b makes the sound horizon at decoupling shorter: ω_b slows down the sound velocity; ω_m speeds up the expansion at a given temperature, so the universe cools to the recombination temperature in less time.

The other quantity determining the angular size of the sound horizon at recombination is the angular diameter distance, given by (Hogg, 1999):

$$D_\mathrm{A} = \begin{cases} \frac{c}{H_0}\,\frac{1}{\sqrt{\Omega_K}}\,\sinh\left[\sqrt{\Omega_K}\,\int_0^z \frac{dz'}{E(z')}\right] & \text{for } \Omega_K > 0 \\ \frac{c}{H_0}\,\int_0^z \frac{dz'}{E(z')} & \text{for } \Omega_K = 0 \\ \frac{c}{H_0}\,\frac{1}{\sqrt{|\Omega_K|}}\,\sin\left[\sqrt{|\Omega_K|}\,\int_0^z \frac{dz'}{E(z')}\right] & \text{for } \Omega_K < 0 \end{cases} \tag{9}$$

where the parameter Ω_K measures the "curvature of space", defined by the relation $\Omega_\mathrm{m}+\Omega_r+\Omega_\Lambda+\Omega_K = 1$, and $E(z) = \left[\Omega_m(1+z)^3 + \Omega_r(1+z)^4 + \Omega_K(1+z)^2 + \Omega_\Lambda\right]^{1/2}$. The maximum contribution to the integral in eq. (9) comes from low redshifts (the quantity $(1+z)/E(z)$ peaks at $1+z_\mathrm{peak} \approx (1/3)\sqrt{6(1-\Omega_K)/\Omega_m}$), so that Ω_r can be neglected in the calculation of the angular diameter distance to the last scattering surface. Hence, $D_\mathrm{A}(z_\mathrm{rec})$ depends on H_0, Ω_m, Ω_Λ and Ω_K. As we have just see, however, the three density parameters are not independent since they obey the relation defining the curvature of space.

The curvature implies that the geodesics are either convergent (closed universe) or divergent (open universe). This makes the CMB pattern at the last scattering surface look larger or smaller, respectively, than the actual size. Thus the angular size of the sound horizon at recombination is a probe of the geometry of the universe. The sound horizon was first clearly seen by WMAP (Hinshaw et al., 2013, their Fig. 12). On the 71% of the sky outside the component separation mask (Planck Collaboration I, 2014, their Fig. 31) have found 11,396 cold spots and 10,468 hot spots, consistent with the ΛCDM *Planck* best fit model prediction of $4\pi\,f_\mathrm{sky}\,\bar{n}_\mathrm{peak} = 11,073$ each. Stacking maps of CMB intensity at the position of the temperature extrema yielded a detection of the sound horizon at recombination with a $95\,\sigma$ significance.

In the standard cosmological model with adiabatic scalar perturbations, temperature hot spots correspond to potential wells (i.e. over-dense regions) at the surface of last scattering. Therefore, matter flows toward these regions. At twice the acoustic horizon scale, the flow of matter is accelerating due to gravity; this creates a radial polarization pattern. At the horizon scale, the flow is decelerating due to the central photon pressure, which creates a tangential pattern. Around cold spots (potential hills), the polarization follows the opposite pattern, with tangential and radial polarization formed at the two scales, respectively.

The stacked *Planck* maps of the Stokes Q and U parameters were rotated in the temperature extrema radial frame $Q_r(\theta)$ and $U_r(\theta)$. In this reference frame the standard model predicts $Q_r(\theta)$ alternating between positive (radial polarization) and

[3] `http://theory.physics.helsinki.fi/~cpt/Cosmo12.pdf`

negative (tangential polarization) values and $U_r(\theta) = 0$. The data are in excellent agreement with the best-fit model Planck Collaboration I (2014, see their Fig. 31).

5.3 Modelling the CMB power spectrum

The CMB power spectrum provides the most important single observational data set for determining (or constraining) cosmological parameters, since it has a rich structure which we can measure with an accuracy that other cosmological observations cannot match. It depends on many different cosmological parameters in many ways. Key features depend on a combination of parameters; one example is the angular scale of the sound horizon, discussed above, that determines the position of the first peak in the power spectrum. As a result, measurement of CMB anisotropies will, in principle, be able to yield strong constraints on combinations of parameters but not on each of them separately. In some cases, the different effects of parameters on the various features of the CMB power spectra allow one to break the degeneracies, but some parameters may be degenerate in the CMB data. Other cosmological observations are then needed to break such degeneracies.

The cosmological interpretation of a measured CMB power spectrum requires, to some extent, the introduction of a particular kind of models. A simple, broad, and well-motivated set of models are associated with primordial inflation. In this scenario the universe is described by a homogeneous and isotropic background with phase-coherent, power-law initial perturbations which evolve freely, with cold dark matter and a cosmological constant. This model space excludes, for example, perturbations caused by topological defects or other "stiff" sources, arbitrary initial power spectra, or any departures from the standard background cosmology.

In this framework the evolution of the perturbations can be computed accurately using a CMB Boltzmann code (the default code used by the *Planck* collaboration is `camb`[4]) once the initial conditions, the ionization history and the constituents of the universe are specified. The baseline model (Planck Collaboration XVI, 2014) assumed purely adiabatic scalar perturbations at very early times, with a (dimensionless) curvature power spectrum parameterized by

$$\mathcal{P}_{\mathcal{R}}(k) = A_{\rm s} \left(\frac{k}{k_0}\right)^{n_{\rm s}-1+(1/2)(dn_{\rm s}/d\ln k)\ln(k/k_0)} , \tag{10}$$

where the "running" of the spectral index, $\mathrm{d}n_s/\mathrm{d}\ln k$, describes departures of the scalar perturbations from a power law with spectral index $n_{\rm s}$; $n_{\rm s}$ and $dn_{\rm s}/d\ln k$ were taken to be constant. The pivot scale, k_0, was chosen to be $k_0 = 0.05\,\mathrm{Mpc}^{-1}$, roughly in the middle of the logarithmic range of scales probed by *Planck*. With this choice, $n_{\rm s}$ is not strongly degenerate with the amplitude parameter $A_{\rm s}$.

An alternative measure of the normalization of the power spectrum of primordial perturbations, often used in the literature particularly in studies of large-scale structure, is denoted as σ_8. This is the rms fluctuation in total matter (baryons + cold dark matter + massive neutrinos) in $8\,h^{-1}$ Mpc spheres at $z = 0$, computed in linear theory. It is related to the dimensionless matter power spectrum, $\mathcal{P}_{\rm m}$, by

$$\sigma_R^2 = \int \frac{dk}{k}\, \mathcal{P}_{\rm m}(k) \left[\frac{3j_1(kR)}{kR}\right]^2 , \tag{11}$$

[4] `http://camb.info`

where $R = 8\,h^{-1}\,\mathrm{Mpc}$ and j_1 is the spherical Bessel function of order 1.

The *Planck* collaboration also considered extended models including primordial tensor modes (gravitational waves). The (dimensionless) tensor mode power spectrum was parameterized as a power-law with

$$\mathcal{P}_{\rm t}(k) = A_{\rm t}\left(\frac{k}{k_0}\right)^{n_{\rm t}}. \tag{12}$$

As usual in the literature, the parameter used in the analysis was not $A_{\rm t}$ but $r_{0.05} \equiv A_{\rm t}/A_{\rm s}$, the primordial tensor-to-scalar ratio at $k = k_0$. However constraints at $k = 0.002\,\mathrm{Mpc}^{-1}$ (denoted $r_{0.002}$) were also reported. Actually, most previous CMB experiments have provided constraints at this scale, where there is some sensitivity to tensor modes in the large-angle temperature power spectrum.

The *Planck* data are only weakly sensitive to the tensor spectral index, $n_{\rm t}$ (which is assumed to be close to zero); therefore the theoretically motivated single-field inflation consistency relation $n_{\rm t} = -r_{0.05}/8$, was adopted, rather than varying $n_{\rm t}$ independently.

To make accurate predictions for the CMB power spectra, the background ionization history has to be calculated to high accuracy. There are now accurate and fast codes (`HyRec`[5], `CosmoRec`[6]) that take into account many relevant atomic transitions and processes that can affect the details of the recombination process. The *Planck* collaboration used the faster code `recfast`[7] with appropriately chosen small correction functions calibrated to the full numerical results.

The code should accurately capture the ionization history until the universe is reionized at late times, probably by ultra-violet photons from massive stars. The CMB power spectrum is affected by the total column density of free electrons along each line of sight, parameterized by its Thomson scattering optical depth τ due to the reionization. Simple reionization models were used by Planck Collaboration XVI (2014) and (Planck Collaboration XIII, 2016), while a more refined model was used in the most recent analysis (Planck Collaboration Int. XLVII, 2016). However, the CMB large-scale polarization anisotropies are very weakly sensitive to the detailed reionization history. They are mainly sensitive to the overall value of the optical depth, which determines the amplitude of the reionization bump in the EE power spectrum (see Section 6) and is one of the parameters of the baseline ΛCDM cosmological model.

As for the contents of the universe, the *Planck* collaboration assumed, for the baseline model, that the cold dark matter is pressureless, stable and non-interacting, with a physical density $\omega_{\rm c} \equiv \Omega_{\rm c}h^2$. The baryons, with density $\omega_{\rm b} \equiv \Omega_{\rm b}h^2$, are assumed to consist almost entirely of hydrogen and helium; the mass fraction in helium was parameterized by $Y_{\rm P}$. The additional energy density in neutrinos was accounted for by assuming that they have a thermal distribution with an effective energy density

$$\rho_\nu = N_{\rm eff}\,\frac{7}{8}\left(\frac{4}{11}\right)^{4/3}\rho_\gamma, \tag{13}$$

with $N_{\rm eff} = 3.046$ in the baseline model. This density is divided equally between three neutrino species while they remain relativistic. However, $N_{\rm eff}$ was allowed to vary and is a parameter of the model. The sum of neutrino masses, in eV, is indicated

[5] `http://www.sns.ias.edu/~yacine/hyrec/hyrec.html`
[6] `http://www.chluba.de/CosmoRec/`
[7] `http://www.astro.ubc.ca/people/scott/recfast.html`

by $\sum m_\nu$ and is another parameter. The possibility of extra radiation, beyond that included in the Standard Model, was also considered. This was modeled as additional massless neutrinos contributing to the total $N_{\rm eff}$ determining the radiation density.

In the baseline model the dark energy is accounted for as a cosmological constant with current density parameter Ω_Λ. But a dynamical dark energy component was also considered. Its equation of state was parameterized either as a constant w or as a function of the cosmological scale factor, $a = (1+z)^{-1}$, with

$$w(a) \equiv \frac{p}{\rho} = w_0 + (1-a)w_a. \tag{14}$$

It was assumed that the dark energy does not interact with other constituents other than through gravity.

Planck Collaboration XVI (2014) noted a mild preference for the amplitude of the CMB lensing signal to be slightly higher than expected from the standard model and quantified this introducing by an additional parameter, $A_{\rm L}$. Another parameter, $m^{\rm eff}_{\nu,\,\rm sterile}$, was introduced to take into account the possibility of the presence of sterile neutrinos, hypothetical particles that interact only via gravity and do not interact via the weak interaction like the known neutrinos. In summary, the *Planck* analysis of the CMB power spectrum allowed the following 16 parameters to vary:

- the baryon density $\omega_{\rm b} \equiv \Omega_{\rm b} h^2$;
- the cold dark matter density $\omega_{\rm c} \equiv \Omega_{\rm c} h^2$;
- the CosmoMC approximation to the angular scale of the sound horizon at $z = z_*$, $r_*/D_{\rm A}(z_*)$, $\theta_{\rm MC}$, where $D_{\rm A}(z)$ is the angular diameter distance;
- the Thomson scattering optical depth due to reionization, τ;
- the power-law index of the spectrum of scalar perturbations at the pivot scale $k_0 = 0.05{\rm Mpc}^{-1}$, $n_{\rm s}$;
- the log amplitude of the primordial curvature perturbations at $k_0 = 0.05\,{\rm Mpc}^{-1}$, $\ln(10^{10} A_{\rm s})$;
- the curvature parameter today Ω_K ($\Omega_{\rm tot} = 1 - \Omega_K$);
- the sum of neutrino masses in eV, $\sum m_\nu$;
- the effective mass of sterile neutrino in eV, $m^{\rm eff}_{\nu,\,\rm sterile}$;
- the leading term, w_0, of the dark energy equation of state: $w(a) = w_0 + (1-a)w_a$; the case of a constant equation of state with $w = w_0$ was also considered;
- the first order perturbation of the dark energy equation of state, w_a;
- the effective number of neutrino-like relativistic degrees of freedom, $N_{\rm eff}$;
- the fraction of baryonic mass in helium, $Y_{\rm P}$;
- the amplitude of the lensing power relative to the physical value, $A_{\rm L}$;
- the running of the spectral index, $dn_{\rm s}/d\ln k$;
- the ratio of tensor primordial power to curvature power at $k_0 = 0.05\,{\rm Mpc}^{-1}$, $r_{0.05}$.

The first 6 parameters ($\omega_{\rm b}$, $\omega_{\rm c}$, $\theta_{\rm MC}$, τ, $n_{\rm s}$ and $A_{\rm s}$) define the standard spatially-flat ΛCDM cosmology with a power-law spectrum of adiabatic scalar perturbations, referred to as "base ΛCDM" in *Planck* papers. The other parameters represent extensions of the "base" model.

Many other parameters could be derived from those listed above. These include, among others (Planck Collaboration XVI, 2014; Planck Collaboration XIII, 2016):

- the dark energy density, Ω_Λ;
- the age of the Universe today (in Gyr), t_0;
- the total matter density (including massive neutrinos) today, $\Omega_{\rm m}$;
- the rms matter fluctuations today in $8\,h^{-1}$ Mpc spheres in linear theory, σ_8;
- the primordial spectral index of the curvature perturbations at wavenumber $k = 0.002\,{\rm Mpc}^{-1}$, $n_{\rm s,0.002}$ (the default pivot scale is $k = 0.05\,{\rm Mpc}^{-1}$, so that $n_{\rm s} \equiv n_{\rm s,0.05}$);
- the redshift at which Universe is half reionized (for a given reionization history), $z_{\rm re}$;
- the current value of the Hubble parameter in ${\rm km\,s^{-1}Mpc^{-1}}$, H_0;
- the ratio of tensor primordial power to curvature power at $k_0 = 0.002\,{\rm Mpc}^{-1}$, $r_{0.002}$;
- the redshift for which the optical depth equals unity, from recombination only (no reionization), z_*;
- the comoving size of the sound horizon at $z = z_*$, $r_* = r_{\rm s}(z_*)$;
- the angular size of the sound horizon at $z = z_*$ ($r_*/D_{\rm A}$), θ_*;
- the redshift at which the baryon-drag optical depth (from recombination only, no reionization) equals unity, i.e. when Compton drag balances the gravitational force, $z_{\rm drag}$;
- the comoving size of the sound horizon at $z = z_{\rm drag}$, $r_{\rm drag} = r_{\rm s}(z_{\rm drag})$; this is an important scale, often used in studies of baryon acoustic oscillations;
- the comoving characteristic damping wavenumber (${\rm Mpc}^{-1}$), $k_{\rm D}$;
- the angular extent of photon diffusion at last scattering (angular damping scale), $\theta_{\rm D} = \pi/[k_{\rm D} D_{\rm A}(z_*)]$;
- the redshift of matter-radiation equality, $z_{\rm eq}$, assuming that neutrinos are fully relativistic (i.e. that their mass can be neglected) at this epoch;
- the comoving wavenumber of the perturbation mode that entered the Hubble radius at matter-radiation equality $z_{\rm eq}$, $k_{\rm eq} \equiv H(z_{\rm eq})/(1 + z_{\rm eq})$;
- the angular size of the horizon at matter-radiation equality, $\theta_{\rm eq}$;
- the angular scale of the sound horizon at matter-radiation equality, $\theta_{\rm s,eq} \equiv r_{\rm s}(z_{\rm eq})/D_{\rm A}(z_*)$, where $r_{\rm s}$ is the sound horizon and z_* is the redshift of last scattering;

- the present day baryon density, $\Omega_{\rm b}$;
- the power-law spectral index of inflation tensor perturbations at $k_0 = 0.05\,{\rm Mpc}^{-1}$, $n_{\rm t} = -r_{0.05}/8$;
- the helium nucleon fraction defined by $Y_{\rm P}^{\rm BBN} \equiv 4n_{\rm He}/n_{\rm b}$;
- the comoving angular diameter distance to last scattering, $D_{\rm A}(z_*)$;
- various quantities reported by Baryon Acoustic Oscillation (BAO) and redshift-space distortion measurements.

5.4 Effect of cosmological parameters on the CMB power spectrum

Let us finally consider the total effect of the various cosmological parameters on the CMB power spectrum. On super-horizon scales the temperature in any given direction depends only on gravity, i.e. on the fluctuations, $\phi(\vec{r})$, of the gravitational potential:

$$\frac{\Delta T}{T}(\vec{r}) = \frac{1}{3}\phi(\vec{r}). \tag{15}$$

For a power-law spectrum of density perturbations, $P(k) \propto k^n$, we have

$$\phi \propto k^{(n-1)/2}. \tag{16}$$

Hence the slope of the power spectrum on super-horizon scales is a measure of the slope of the power spectrum of primordial perturbations. For a spectrum close to Harrison-Zeldovich ($n = 1$), as expected from primordial inflation, the CMB power spectrum,

$$\langle \Delta T^2 \rangle \propto D_\ell \propto \ell(\ell+1)C_\ell \propto \ell^{(n-1)/2} \tag{17}$$

is approximately scale-independent. This is indeed seen in the observed power spectrum (Sachs-Wolfe plateau). The plateau however is not perfectly flat, implying n slightly smaller than unity ($n = 0.9667 \pm 0.0040$; Planck Collaboration XIII, 2016).

On sub-horizon scales, the perturbations of the baryon-photon component stop growing and start oscillating in the dark matter potential wells, due to the competing actions of gravity and pressure. These standing waves are called *acoustic oscillations*. We see the amplitude of these (small) fluctuations to be $\Delta T/T \sim 10^{-5}$.

On the contrary, dark matter overdensities continue to grow (slowly during the radiation-dominated epoch, and then faster during the matter-dominated epoch) so that, at recombination, they are much larger than those of the baryon-photon fluid; but we do not see them directly.

At recombination baryons decouple from photons and fall into the dark matter potential wells, thus suddenly increasing their overdensity, while radiation free-streams to us. Thus, *the amplitude of CMB fluctuations directly imply dark matter* and even though both inhomogeneities in the matter and anisotropies in the CMB apparently originated from the same source, these appear very different today.

Both compression and rarefaction contribute to the temperature power spectrum because the sign of ΔT doesn't matter since we are measuring the variance, $(\Delta T)^2$. In the standard model, primordial perturbations are phase-coherent. This means that the wave-modes that complete an odd number of half-oscillations by recombination correspond, at decoupling, to compression in potential wells and rarefaction in potential peaks and give rise to the odd-numbered peaks (1st, 3rd, etc) in the CMB temperature power spectrum (see the lecture slide no. 174).

In particular, the wave-mode that completes half an oscillation by recombination sets the physical scale of the first peak. It is seen as a network of hot and cold spots spaced by the sound horizon. The modes that complete an even number of half-oscillations correspond to rarefaction in potential wells and compression in potential peaks and give rise to the even-numbered peaks (2nd, 4th, etc.).

There is an important difference between odd and even peaks. In the presence of baryons, peaks corresponding to rarefactions in potential wells cannot attain as high an amplitude as compressions because baryons have inertia, and want to stay at the bottoms of potential wells and away from peaks. So this baryon drag results in the odd peaks having higher amplitude than the even peaks by a factor $(1 + 6R)$ (see eqs. (80) and (81) of De Zotti & Negrello, 2015)[8] with

$$R = \frac{\bar{\rho}_b}{\bar{\rho_\gamma} + \bar{p_\gamma}} = \frac{3\bar{\rho}_b}{4\bar{\rho_\gamma}}. \tag{18}$$

Thus the relative heights of the first and of the second peak probe Ω_b through R. R has to be computed at the epoch when oscillations started. This happens at earlier times for shorter wavelength modes. But $R \to 0$ as we go to earlier times, i.e. as we go towards radiation dominance. That's why the third peak is lower than the first peak.

For small enough scales the effect of photon diffusion and the finite thickness of the last scattering surface (which is approximately the photon mean free path at recombination) smooth out the CMB anisotropy. This effect can be characterized by the damping scale $k_{\rm D}$ defined by (Kaiser, 1983; Planck Collaboration XVI, 2014):

$$k_{\rm D}^{-2} = \frac{c}{6} \int dt \, \frac{(1+z)^2}{n_e(z)\sigma_{\rm T}} \, \frac{R^2 + 16(1+R)/15}{(1+R)^2}, \tag{19}$$

where $n_{\rm e}(z)$ is the density of free electrons, $\sigma_{\rm T}$ is the Thomson cross section and the recombination is carried out over the recombination epoch only, without reionization contributions. The angular damping scale is defined as, $\theta_{\rm D} = \pi/(k_{\rm D} D_{\rm A})$, where $D_{\rm A}$ is the comoving angular diameter distance to z_*.

In summary, the dependence of the CMB power spectrum on the 6 parameters ($\omega_{\rm b}$, $\omega_{\rm c}$, $\theta_{\rm MC}$, τ, $n_{\rm s}$ and $A_{\rm s}$) defining the spatially-flat "base ΛCDM" model goes as follows, setting $\omega_m = \omega_{\rm b} + \omega_{\rm c}$:

- the location of the peaks, determined by the angular size of the sound horizon at recombination, $\theta_* = r_*(z_*)/D_{\rm A}(z_*)$, depends on ω_m, $\omega_{\rm b}$ and Ω_Λ;
- the amplitude ratio of odd to even peaks depends on the ratio $\omega_{\rm b}/\omega_\gamma$ and thus gives $\omega_{\rm b}$ since ω_γ is accurately known;
- the redshift of matter/radiation equality, $1 + z_{\rm eq} = \omega_m/\omega_\gamma$ gives ω_m;
- the angular damping scale for photon diffusion, $\theta_{\rm D} = \pi/[k_{\rm D} D_{\rm A}(z_*)]$ depends on ω_m, $\omega_{\rm b}$ and Ω_Λ;
- the global amplitude of the power spectrum gives us the amplitude of the spectrum of primordial curvature perturbations, A_s;

[8] Note that eq. (80) of De Zotti & Negrello (2015) contains a misprint: in the numerator $(1 + 3R)$ must be replaced with $(1 + 6R)$

- the slope of the CMB power spectrum on super-horizon scales (Sachs-Wolfe plateau) is a measure of the slope of the power spectrum of primordial perturbations, n, but is is also slightly affected by the Integrated Sachs-Wolfe (ISW) effect which depends on Ω_Λ (see, e.g., De Zotti & Negrello, 2015);

- the relative amplitude of the CMB power spectrum on large ($\ell \ll 40$) and small ($\ell \gg 40$) angular scales provides constraints on the Thomson scattering optical depth due to reionization, τ. This is because the the primary anisotropies (from recombination) are erased by $\exp(-\tau)$ but only on scales below the horizon at reionization. However, as we shall see, the tightest constraints come from CMB polarization.

Note that, for this model, the Hubble constant is a derived parameter $h = (\omega_m/(1 - \Omega_\Lambda)^{1/2}$. Clearly, to discriminate the effect of each individual parameter on the CMB power spectrum we need to determine it with very high accuracy to detect subtle differences. But even this may not be sufficient and to break some degeneracies it is necessary to resort to external data. Particularly useful in this respect are measurements of Baryon Acoustic Oscillations (BAO), of the Hubble diagram of type Ia supernovae, and of redshift-space distortions.

6 CMB polarization

It is widely recognized in the literature that the CMB polarization is a unique source of information for: i) reionization studies, thanks to the large-scale signature that reionization is expected to leave in the polarization power spectra; for ii) inflation studies, as primordial gravitational waves are expected to produce B-mode CMB polarization and because polarization provides a cleaner probe of initial conditions; and iii) for breaking some degeneracies.

Furthermore, as pointed out by Zaldarriaga et al. (1997) and Galli et al. (2014), cosmic variance limited measurements of the CMB polarization power spectra *alone* have the potential to place stronger constraints on cosmological parameters than measurements of temperature spectra because the acoustic peaks are narrower in polarization and unresolved foreground contributions at high multipoles are much lower in polarization than in temperature.

Since the polarization of CMB anisotropies is generated only by scattering (see Hu & White, 1997, for a pedagogical introduction to the study of CMB polarization), it tracks free electrons and hence isolates the recombination (last-scattering) and reionization epochs (Baumann et al., 2009).

If a free electron 'sees' an isotropic radiation pattern, the scattered radiation remains unpolarized because orthogonal polarization directions cancel out. However, if the incoming radiation field has a quadrupole component, a net linear polarization is generated via Thomson scattering. Before decoupling the polarization is damped out by subsequent scatterings. But the polarization induced by the quadrupole moment at decoupling survives. Hence linear polarization results from the velocities of electrons on scales smaller than the photon diffusion length scale.

The anisotropy field is defined by a 2×2 tensor $I_{ij}(\hat{n})$, where $\hat{n}$ denotes the direction on the sky. The components of I_{ij} are defined relative to two orthogonal basis vectors $\hat{\mathbf{e}}_1$ and $\hat{\mathbf{e}}_2$ perpendicular to $\hat{n}$. Linear polarization is then described by the Stokes parameters $Q = \frac{1}{4}(I_{11} - I_{22})$ and $U = \frac{1}{2}I_{12}$, while the temperature anisotropy is $T = \frac{1}{4}(I_{11} + I_{22})$.

The quantity T is invariant under a rotation in the plane perpendicular to $\hat{n}$ and hence may be expanded in terms of scalar (spin-0) spherical harmonics [eq. (2)]. The quantities Q and U, however, transform under rotation by an angle ψ as a spin-2 field $(Q \pm iU)(\hat{n}) \rightarrow e^{\mp 2i\psi}(Q \pm iU)(\hat{n})$. The harmonic analysis of $Q \pm iU$ therefore requires expansion on the sphere in terms of tensor (spin-2) spherical harmonics (Zaldarriaga & Seljak, 1997; Kamionkowski et al., 1997):

$$(Q + iU)(\hat{n}) = \sum_{\ell,m} a_{\ell m}^{(\pm 2)} \; [{}_{\pm 2}Y_{\ell m}(\hat{n})] \; . \tag{20}$$

Instead of $a_{\ell m}^{(\pm 2)}$ it is convenient to introduce the linear combinations (Newman & Penrose, 1962)

$$a_{\ell m}^{E} \equiv -\frac{1}{2}\left(a_{\ell m}^{(2)} + a_{\ell m}^{(-2)}\right) , \qquad a_{\ell m}^{B} \equiv -\frac{1}{2i}\left(a_{\ell m}^{(2)} - a_{\ell m}^{(-2)}\right) . \tag{21}$$

Then one can define two scalar (spin-0) fields, called E and B modes, instead of the spin-2 quantities Q and U

$$E(\hat{n}) = \sum_{\ell,m} a_{\ell m}^{E} \; Y_{\ell m}(\hat{n}) \, , \qquad B(\hat{n}) = \sum_{\ell,m} a_{\ell m}^{B} \; Y_{\ell m}(\hat{n}) \, . \tag{22}$$

This nomenclature reflects the properties from electrostatics: the E-polarization is *curl-free* ($\nabla \times \mathbf{E} = 0$) with polarization vectors that are radial around cold spots and tangential around hot spots on the sky; the B-polarization is *divergence-free* ($\nabla \cdot \mathbf{B} = 0$) but has a *curl*: its polarization vectors have vorticity around any given point on the sky. E and B are both invariant under rotations, but behave differently under parity transformations. When reflected about a line going through the center, the E-patterns remain unchanged, while the B-patterns change sign.

The local distinction between the two modes is that the polarization direction is aligned with the principal axes of the polarization amplitude for E and crossed (45 degrees) for B. Thus, while the description of the polarization pattern by the Stokes parameters depends on an arbitrary choice of coordinates, the E and B modes allow us to describe it by its orientation relative to itself.

The symmetries of temperature and polarization (E- and B-mode) anisotropies allow four types of correlations: the autocorrelations of temperature fluctuations and of E- and B-modes denoted by TT, EE, and BB, respectively, plus the cross-correlation between temperature fluctuations and E-modes, TE. The other correlations (TB and EB) vanish for symmetry reasons unless there is a parity-violating processes in the early universe. So, non-zero TB and EB correlations would be a signature of such new physics.

The dependence on cosmological parameters of each of these spectra differs. Therefore a combined measurement of all of them improves the constraints on cosmological parameters by increasing the statistics and by removing degeneracies between fitted parameters. This obviously helps in discriminating between cosmological models.

Kamionkowski et al. (1997) and Zaldarriaga et al. (1997) demonstrated the cosmological significance of the E/B decomposition of CMB polarization showing that: i) scalar (density) perturbations create only E-modes and *no* B-modes; ii) vector (vorticity) perturbations create mainly B-modes; iii) tensor (gravitational wave) perturbations create both E-modes and B-modes. Vector perturbations decay with the expansion of the universe and are therefore generally neglected. However it is worth

noting that cosmic strings can produce a B-mode signal via vector modes (e. g. Seljak et al., 1997).

These these results can be understood as follows. Density perturbations only generate polarization parallel to the direction of the plane wave, i.e. E-mode polarization. Since free streaming (to linear order) projects a curl-free spatial pattern to a curl-free angular distribution, the observed signal from scalar perturbations remains curl-free and hence pure E-mode. The spatial pattern of the polarization field generated by tensor perturbations has non-zero curl. Therefore its projection produces B-mode polarization. The fact that scalars do not produce B-modes while tensors do is the basis for the often-quoted statement that detection of B-modes is a smoking gun of tensor modes, and therefore of inflation. For this reason the detection of the primordial B-mode is considered the "holy grail" of observational cosmology.

6.1 Lensing B-mode

Note, however, that the above statements apply to primary anisotropies only. The weak gravitational lensing of the CMB due to the intervening matter distribution converts E-modes to the B-modes (also generating non-zero TB and EB-correlations), in addition to smoothing the acoustic oscillations of the power spectra of temperature and E-mode anisotropies and of adding power at $\ell \gtrsim 3000$.

The effect of weak gravitational lensing can be described as a remapping of the primordial unlensed CMB field by large scale density fluctuations that induce random deflections in the direction of the CMB photons as they propagate from the last scattering surface to us. The displacement angle is related to the projected surface density or, equivalently, the projected gravitational potential. Although the remapping does not mix Q and U, it nevertheless results in a mixing of the E and B modes because the transformation from (Q, U) to (E, B) is non-local (Smith et al., 2009). In particular, E-mode power will be transferred into B modes, generating in this way the largest guaranteed B-mode signal. This signal is totally independent from the existence of primordial B modes, i.e. the existence of tensor modes in the early universe. Since for realistic values of r, this B-mode lensing signal dominates over the primordial one at sub-degree scales, to recover the primordial B-mode the signal must be "delensed" (Smith et al., 2009, and references therein).

While, on one side, the lensing B-mode is a contaminant when trying to measure r, on the other side it contains key cosmological information (Smith et al., 2009, and references therein). In fact, it is sensitive to both the geometry of the universe and to the growth of structure at moderate redshift ($z \lesssim 5$), thus helping to break the degeneracy among parameters determining the angular diameter distance. Moreover, since it is sensitive to the expansion history of the universe between recombination and moderate redshifts, it probes the evolution of the equation of state of the dark energy. It also maps the distribution of matter on large scales and high redshifts where density fluctuations are still in the linear regime and are thus robust cosmological probes. Furthermore, since the lensing B-modes allow for an order of magnitude extension to smaller scales of the lensing potential as compared to temperature lensing, it is uniquely sensitive to parameters that affect structure formation in the late universe, such as neutrino masses.

The effects of lensing in polarization data was first detected by ground-based experiments (Hanson et al., 2013; Ade et al., 2014; van Engelen et al., 2015). *Planck* has achieved a $40\,\sigma$ measurement of the CMB lensing potential using temperature

and polarization data; using a polarization-only estimator, lensing was detected at a significance of $5\,\sigma$ (Planck Collaboration XV, 2016).

The separation of the primordial and lensing B-modes is eased by the different characteristic scales. The lensing B-mode power spectrum peaks on relatively small scales ($\ell \simeq 1000$) because the matter distribution is only weakly correlated on larger scales. On the contrary, the anisotropy power spectra due to tensor perturbations fall sharply on scales that are sub-Hubble at recombination ($\ell > 60$) since the amplitude of gravitational waves decays away as $(1 + z)$ inside the Hubble radius (oscillations are damped because gravitational waves are very weakly coupled to photons). This seriously limits the power of temperature anisotropies to constrain gravitational waves since the sampling variance of the dominant scalar perturbations is large at low ℓ's. But the CMB B-mode polarization provides an alternative route to detecting the effect of gravitational waves on the CMB which is not limited by cosmic variance.

6.2 Primordial B-mode

The primordial signal is very weak, with r.m.s. $= 0.18\sqrt{r/0.2}\,\mu$K (Challinor & Peiris, 2009) but next generation CMB polarization experiments can reach $r \lesssim 0.001$ (e. g., Ishino et al., 2016). Probably the main problem will be the removal of polarized foregrounds down to nK levels.

There are two characteristic scales for attempting detection of primordial B-modes: the reionization signal at $\ell < 10$ (see below), and the signal from recombination at $\ell < 100$. Detection of primordial tensor perturbations would probe physics at an energy *twelve orders of magnitude* larger than the center of mass energy at the Large Hadron Collider (LHC). A detection or constraint on the tensor-to-scalar ratio r will answer a fundamental question about the range of the scalar field excursion, $\Delta\phi$, during inflation as compared to the Planck mass scale $M_{\rm Pl}$. The quantity $\Delta\phi/M_{\rm Pl}$ is sensitive to the physics behind inflation.

It is thus understandable that the announcement of the detection of the primordial B-mode polarization by the Background Imaging of Cosmic Extragalactic Polarization 2 (BICEP2) collaboration (BICEP2 Collaboration, 2014) has sparked a great excitement. However, a crucial step in the interpretation of the signal they detected at $50 < \ell < 150$ at a single frequency (150 GHz) was excluding an explanation based on polarized thermal dust emission from our Galaxy. The BICEP2 team used a number of models of polarized dust emission to conclude that its power was a factor of ~ 5–10 smaller than the detected signal and inferred a value of the tensor-to-scalar ratio $r = 0.20^{0.07}_{-0.05}$. However, at the time relevant observational data on polarized dust emission were lacking, and their modelling involved a high degree of extrapolation.

The BICEP2 interpretation of the signal was later cast in doubt by *Planck* measurements of Galactic dust polarization at 353 GHz (Planck Collaboration Int. XIX, 2015; Planck Collaboration Int. XXII, 2015), which showed that the polarization fraction is higher than expected in regions of low dust emission and characterized the frequency dependence of dust emission intensity and polarization. Planck Collaboration Int. XXX (2016) released information on dust polarization at high Galactic latitude and in particular examined a field centered on the BICEP2 region (but somewhat larger than it). Extrapolating the *Planck* B-mode power spectrum of dust polarization at 353 GHz over the multipole range $40 < \ell < 120$ to 150 GHz, they showed that the B-mode polarization signal detected by BICEP2 could be entirely

due to dust, although the level of polarized dust emission was measured with relatively low signal-to-noise ratio.

A BICEP2/Keck Array-*Planck* joint analysis (BICEP2/Keck and Planck Collaborations, 2015) combined the high sensitivity B-mode maps from BICEP2 and Keck Array with the *Planck* maps at higher frequencies where dust emission dominates. A study of the cross-correlations of all these maps in the BICEP2 field did not find any statistically significant evidence for primordial gravitational waves, setting an upper limit of $r_{0.05} < 0.12$ at 95 % confidence level.

Most recently BICEP2 Collaboration & Keck Array Collaboration (2016) analyzed all data taken by the BICEP2 and Keck Array cosmic CMB polarization experiments including the first Keck Array observations at 95 GHz and computed the auto- and cross-spectra between these maps and the publicly available maps from WMAP and *Planck* at frequencies from 23 to 353 GHz. An excess over expectations from the ΛCDM model including lensing was detected at modest significance in the $95 \times 150\,\mathrm{GHz}$ BB spectrum, consistent with the dust contribution. This analysis yielded a largely model independent upper limit $r_{0.05} < 0.09$ at 95% confidence level. Combining these results with the (more model-dependent) constraints from *Planck* analysis of CMB temperature plus baryon acoustic oscillations and other data yielded a combined limit $r_{0.05} < 0.07$ at 95% confidence level.

6.3 E-mode and TE power spectra and constraints on the reionization history

There is a long list of ground-based and balloon experiments that have measured E-mode auto power spectra (EE) and/or TE cross spectra[9]. WMAP has measured the TE power spectrum up to $\ell \simeq 1000$ and the EE spectrum for $2 \leq \ell \leq 7$. Planck Collaboration XI (2016) have reported accurate determinations of both the TE and the EE power spectra up to $\ell \simeq 2000$, although at high multipoles residual systematic errors were detected in the E polarization, typically at the $\mu\mathrm{K}^2$ level. The combined analysis of temperature and polarization data has not detected any significant deviation from the standard ΛCDM model, further establishing its robustness. Several non-minimal cosmological models were investigated but no significant evidence for extra physical ingredients was found. This represents an important milestone set by the *Planck* satellite.

The E-mode power peaks around $\ell \sim 1000$, corresponding to the angle subtended by the width of the visibility function at recombination. On larger scales the polarization probes the electron-baryon velocity at last scattering. Asymptotically, the photon-baryon overdensity oscillates as a cosine, and the peculiar velocity of the plasma as a sine (the velocity is maximum, in absolute value, when the over/underdensity is at a minimum, and vice-versa). The peaks in the E-mode spectrum therefore coincide with the troughs of the temperature spectrum. Large-angle polarization from the last-scattering surface is very small since the generation of a quadrupole in the temperature anisotropy occurs via causal physics (photon diffusion) that is suppressed outside the horizon.

When the first sources of ionizing radiation re-ionize cosmic hydrogen, the resulting free electron density can re-scatter CMB photons. For polarization, re-scattering suppresses the signal from recombination by a factor $e^{-\tau}$, where τ is the Thomson scattering optical depth due to reionization. But it also produces a new bump in the

[9]See `https://lambda.gsfc.nasa.gov/product/expt/` for an exhaustive list of CMB anisotropy experiments, including those with polarization capability

polarization power spectra on the horizon scale at reionization, which obviously has an angular size much larger than that at recombination and therefore shows up at low ℓ's. The strength of this large-angle polarization varies almost linearly with τ and is therefore a measure of it (Challinor & Peiris, 2009).

The multipole at which the reionization bump in the EE, TE and (for tensor perturbations) BB peaks is controlled by the epoch of reionization, $z_{\rm re}$. A fitting formula was given by Liu et al. (2001):

$$\ell_{\rm peak} \simeq 0.74(1+z_{\rm re})^{0.73}\Omega_m^{0.11}, \tag{23}$$

where Ω_m is the matter (baryons + dark matter) density in units of the critical density.

The characterization of the reionization bump in the polarization power spectra and, as a consequence, the derivation of τ, proved to be challenging. This is because the expected level of the E-mode polarization power spectrum at low multipoles ($\ell < 10$) is only a few times $10^{-2}\,\mu{\rm K}^2$, lower by more than two orders of magnitude than the level of the temperature anisotropy power spectrum. For such weak signals the difficulty is not only to have enough detector sensitivity, but also to reduce and control both instrumental systematic effects and foreground residuals to a very low level. The history of τ estimates is summarized in Planck Collaboration Int. XLVII (2016).

The bump in the TE power spectrum is stronger but the constraints on τ that can be derived are weaker. This is because the cosmic variance for TE is larger, due to the contribution of the temperature term (see Fig. 3 of Planck Collaboration Int. XLVII, 2016). Also the dependence of TE on τ is intrinsically weaker ($\propto \tau$ compared with τ^2 for EE) and there is only partial correlation between T and E.

Since the reionization signal shows up on large angular scales, it cannot be detected by ground based or balloon-borne surveys that can cover limited areas of the sky. The WMAP mission was the first to extract a τ measurement through the correlation between the temperature field and the E-mode polarization (i.e., the TE power spectrum). The analysis of the first year WMAP data gave a value of $\tau = 0.17 \pm 0.04$, suggesting a reionization redshift, $z_{\rm re}$, between 11 and 30, in conflict with measurements of the Gunn–Peterson absorption trough in spectra of distant quasars, which showed neutral hydrogen present in the intergalactic medium at $z \sim 6$ (Fan et al., 2006).

The optical/UV data on the evolution of the the cosmic star formation rate indicate that the production of ionizing photons can hardly surpass the recombination rate at $z \gtrsim 7$–8. This led to the speculation of a "double reionization" process, with additional sources of ionizing photons at high redshift (e. g., Cen, 2003).

In the 3-year WMAP release, τ was revised down to 0.10 ± 0.03 using E-modes alone, whereas the combined TT, TE, and EE power spectra gave 0.09 ± 0.03. The subsequent WMAP surveys led to improvements of the error bars, ending up with $\tau = 0.089 \pm 0.014$ after the 9-year release. In the instantaneous reionization model, this implies $z_{\rm re} \simeq 10.4$, still requiring an early production of ionizing photons much in excess of expectations from the cosmic star formation history.

The first *Planck* cosmological results were based on *Planck* temperature power spectra combined with the polarized WMAP data and gave the same value, $\tau = 0.089 \pm 0.014$. However, using a preliminary version of the *Planck* 353 GHz polarization maps to clean the dust emission (in place of the WMAP dust model), the optical depth was reduced by approximately $1\,\sigma$ to $\tau = 0.075 \pm 0.013$.

The next step was the use of the *Planck*/LFI low-resolution polarization maps at 70 GHz. The foreground cleaning was performed using the LFI 30 GHz and the *Planck*/HFI 353 GHz maps as polarized synchrotron and dust templates, respectively. The optical depth was found to be $\tau = 0.078 \pm 0.019$, and this decreased to 0.066 ± 0.016 when adding CMB lensing data.

Most recently Planck Collaboration Int. XLVI (2016) managed to identify, model and remove previously unexplained systematic effects in the HFI polarization data on large angular scales. These improvements allowed the determination of τ using, for the first time, the low-multipole EE data from HFI, reducing significantly the central value and uncertainty.

Planck Collaboration Int. XLVII (2016) combined the *Planck* CMB anisotropy data in temperature with the low-multipole polarization data to fit ΛCDM models with various parameterizations of the reionization history. They obtained $\tau = 0.058 \pm 0.012$ for the instantaneous reionization model. The average redshift at which reionization occurs was found to lie between $z = 7.8$ and 8.8, depending on the model of reionization adopted.

As already mentioned, observations of the Gunn-Peterson effect in quasar spectra (Fan et al., 2006) have shown that the intergalactic gas became almost fully reionized by redshift $z \simeq 6$. Star-forming galaxies at redshifts $z > 6$ are believed to be the most likely sources of reionization, given that the abundance of active galactic nuclei (AGN) declines beyond $z \sim 3$ (Willott et al., 2010; McQuinn, 2016). But several optical/UV measures of the neutrality of the intergalactic hydrogen and of the ionizing photon production by high-z star-forming galaxies consistently indicate that it quickly increases above $z \simeq 6$ (Robertson et al., 2015), implying $\tau \lesssim 0.06$–0.07 (Cai et al., 2014). To account for higher values of τ some 'exotic' sources acting at higher redshifts must be invoked, such as decays/annihilations of dark matter particles, enhanced structure formation, or mini-quasars powered by intermediate mass black holes.

The latest *Planck* estimate of τ may be consistent with reionization driven by high-z star-forming galaxies. Recent analyses have shown that it is possible to create a self-consistent model for the reionization of the universe using the observed galaxy population as a basis (Cai et al., 2014; Robertson et al., 2015; Bouwens, 2016). There are, however, still substantial uncertainties on critical parameters, such as the faint end of the UV luminosity function of high-z galaxies, the evolution in the production efficiency of ionizing photons with cosmic time and in the fraction of them that can escape into the intergalactic medium. In any case, the *Planck* result strongly reduces the need for a significant contribution of ionizing photons by 'exotic' sources.

Acknowledgements. I'm deeply grateful to the organizers of the School, and particularly to Agnieszka Pollo, Piotr Flin, Janusz Krywult and Monika Biernacka, for their extraordinarily warm hospitality and constant help. Work supported in part by ASI/INAF Agreement 2014-024-R.0 for the *Planck* LFI activity of Phase E2.

References

Ade, P. A. R., et al., *Measurement of the Cosmic Microwave Background Polarization Lensing Power Spectrum with the POLARBEAR Experiment*, *Physical Review Letters* **113**, 2, 021301 (2014), 1312.6646

Baumann, D., et al., *Probing Inflation with CMB Polarization*, in S. Dodelson, D. Baumann, A. Cooray, J. Dunkley, A. Fraisse, M. G. Jackson, A. Kogut, L. Krauss, M. Zaldarriaga,

K. Smith (eds.) American Institute of Physics Conference Series, *American Institute of Physics Conference Series*, volume 1141, 10–120 (2009), 0811.3919

Bennett, C. L., et al., *First-Year Wilkinson Microwave Anisotropy Probe (WMAP) Observations: Foreground Emission*, ApJS **148**, 97 (2003), astro-ph/0302208

Bennett, C. L., et al., *Nine-year Wilkinson Microwave Anisotropy Probe (WMAP) Observations: Final Maps and Results*, ApJS **208**, 20 (2013), 1212.5225

Bersanelli, M., et al., *COBRAS/SAMBA: report on phase A study*, Technical Report D/SCI(96)3, ESA (1996), http://sci.esa.int/planck/24747

Bersanelli, M., et al., *Planck pre-launch status: Design and description of the Low Frequency Instrument*, A&A **520**, A4 (2010), 1001.3321

BICEP2 Collaboration, *Detection of B-Mode Polarization at Degree Angular Scales by BICEP2*, *Physical Review Letters* **112**, 24, 241101 (2014), 1403.3985

BICEP2 Collaboration, Keck Array Collaboration, *Improved Constraints on Cosmology and Foregrounds from BICEP2 and Keck Array Cosmic Microwave Background Data with Inclusion of 95 GHz Band*, *Physical Review Letters* **116**, 3, 031302 (2016), 1510.09217

BICEP2/Keck and Planck Collaborations, *Joint Analysis of BICEP2/Keck Array and Planck Data*, *Physical Review Letters* **114**, 10, 101301 (2015), 1502.00612

Bouwens, R., *High-Redshift Galaxy Surveys and the Reionization of the Universe*, in A. Mesinger (ed.) Understanding the Epoch of Cosmic Reionization: Challenges and Progress, *Astrophysics and Space Science Library*, volume 423, 111 (2016), 1511.01133

Cai, Z.-Y., et al., *A Physical Model for the Evolving Ultraviolet Luminosity Function of High Redshift Galaxies and their Contribution to the Cosmic Reionization*, ApJ **785**, 65 (2014), 1403.0055

Cardoso, J.-F., et al., *Component Separation With Flexible Models – Application to Multichannel Astrophysical Observations*, *IEEE Journal of Selected Topics in Signal Processing* **2**, 735 (2008)

Cen, R., *The Implications of Wilkinson Microwave Anisotropy Probe Observations for Population III Star Formation Processes*, ApJ **591**, L5 (2003), astro-ph/0303236

Challinor, A., Peiris, H., *Lecture notes on the physics of cosmic microwave background anisotropies*, in M. Novello, S. Perez (eds.) American Institute of Physics Conference Series, *American Institute of Physics Conference Series*, volume 1132, 86–140 (2009), 0903.5158

Davies, R. D., et al., *A determination of the spectra of Galactic components observed by the Wilkinson Microwave Anisotropy Probe*, MNRAS **370**, 1125 (2006), astro-ph/0511384

de Oliveira-Costa, A., et al., *The Quest for Microwave Foreground X*, ApJ **606**, L89 (2004), astro-ph/0312039

De Zotti, G., Negrello, M., *Spectral distortions and anisotropies of the Cosmic Microwave Background*, in M. Biernacka, K. Bajan, G. Stachowski, P. Flin (eds.) Introduction to Cosmology, 15–50 (2015)

De Zotti, G., et al., *Polarization fluctuations due to extragalactic sources*, New A **4**, 481 (1999), astro-ph/9908058

De Zotti, G., et al., *Extragalactic sources in Cosmic Microwave Background maps*, J. Cosmology Astropart. Phys. **6**, 018 (2015), 1501.02170

Delabrouille, J., et al., *A full sky, low foreground, high resolution CMB map from WMAP*, A&A **493**, 835 (2009), 0807.0773

Draine, B. T., Lazarian, A., *Diffuse Galactic Emission from Spinning Dust Grains*, ApJ **494**, L19 (1998), astro-ph/9710152

Eriksen, H. K., et al., *Cosmic Microwave Background Component Separation by Parameter Estimation*, ApJ **641**, 665 (2006), astro-ph/0508268

Eriksen, H. K., et al., *Joint Bayesian Component Separation and CMB Power Spectrum Estimation*, ApJ **676**, 10-32 (2008), 0709.1058

Fan, X., Carilli, C. L., Keating, B., *Observational Constraints on Cosmic Reionization*, ARA&A **44**, 415 (2006), astro-ph/0602375

Fernández-Cobos, R., Vielva, P., Barreiro, R. B., Martínez-González, E., *Multiresolution internal template cleaning: an application to the Wilkinson Microwave Anisotropy Probe 7-yr polarization data*, MNRAS **420**, 2162 (2012), 1106.2016

Fixsen, D. J., Mather, J. C., *The Spectral Results of the Far-Infrared Absolute Spectrophotometer Instrument on COBE*, ApJ **581**, 817 (2002)

Galli, S., et al., *CMB polarization can constrain cosmology better than CMB temperature*, Phys. Rev. D **90**, 6, 063504 (2014), 1403.5271

Greason, M., et al., *Wilkinson Microwave Anisotropy Probe (WMAP): Nine–Year Explanatory Supplement*, Technical report, NASA/GSFC (2012), http://lambda.gsfc.nasa.gov/

Greaves, J. S., Holland, W. S., Friberg, P., Dent, W. R. F., *Polarized CO Emission from Molecular Clouds*, ApJ **512**, L139 (1999), astro-ph/9812428

Hanson, D., et al., *Detection of B-Mode Polarization in the Cosmic Microwave Background with Data from the South Pole Telescope*, *Physical Review Letters* **111**, 14, 141301 (2013), 1307.5830

Haslam, C. G. T., Salter, C. J., Stoffel, H., Wilson, W. E., *A 408 MHz all-sky continuum survey. II - The atlas of contour maps*, A&AS **47**, 1 (1982)

Hinshaw, G., et al., *Nine-year Wilkinson Microwave Anisotropy Probe (WMAP) Observations: Cosmological Parameter Results*, ApJS **208**, 19 (2013), 1212.5226

Hogg, D. W., *Distance measures in cosmology*, *ArXiv Astrophysics e-prints* (1999), astro-ph/9905116

Hu, W., White, M., *A CMB polarization primer*, New A **2**, 323 (1997), astro-ph/9706147

Ishino, H., et al., *LiteBIRD: lite satellite for the study of B-mode polarization and inflation from cosmic microwave background radiation detection*, in Society of Photo-Optical Instrumentation Engineers (SPIE) Conference Series, Proc. SPIE, volume 9904, 99040X (2016)

Kaiser, N., *Small-angle anisotropy of the microwave background radiation in the adiabatic theory*, MNRAS **202**, 1169 (1983)

Kamionkowski, M., Kosowsky, A., Stebbins, A., *Statistics of cosmic microwave background polarization*, Phys. Rev. D **55**, 7368 (1997), astro-ph/9611125

Keating, B., Timbie, P., Polnarev, A., Steinberger, J., *Large Angular Scale Polarization of the Cosmic Microwave Background Radiation and the Feasibility of Its Detection*, ApJ **495**, 580 (1998), astro-ph/9710087

Lamarre, J.-M., et al., *Planck pre-launch status: The HFI instrument, from specification to actual performance*, A&A **520**, A9 (2010)

Lazarian, A., Draine, B. T., *Resonance Paramagnetic Relaxation and Alignment of Small Grains*, ApJ **536**, L15 (2000), astro-ph/0003312

Leach, S. M., et al., *Component separation methods for the PLANCK mission*, A&A **491**, 597 (2008), 0805.0269

Liu, G.-C., et al., *Polarization of the Cosmic Microwave Background from Nonuniform Reionization*, ApJ **561**, 504 (2001), astro-ph/0101368

Macellari, N., Pierpaoli, E., Dickinson, C., Vaillancourt, J. E., *Galactic foreground contributions to the 5-year Wilkinson Microwave Anisotropy Probe maps*, MNRAS **418**, 888 (2011), 1108.0205

Martínez-González, E., Diego, J. M., Vielva, P., Silk, J., *Cosmic microwave background power spectrum estimation and map reconstruction with the expectation-maximization algorithm*, MNRAS **345**, 1101 (2003), astro-ph/0302094

McQuinn, M., *The Evolution of the Intergalactic Medium*, ARA&A **54**, 313 (2016), 1512.00086

Mennella, A., et al., *Planck pre-launch status: Low Frequency Instrument calibration and expected scientific performance*, A&A **520**, A5 (2010), 1001.4562

Newman, E., Penrose, R., *An Approach to Gravitational Radiation by a Method of Spin Coefficients*, *J. Math. Phys.* **3**, 566 (1962)

Page, L., et al., *First-Year Wilkinson Microwave Anisotropy Probe (WMAP) Observations: Beam Profiles and Window Functions*, ApJS **148**, 39 (2003), astro-ph/0302214

Planck Collaboration I, *Planck 2013 results. I. Overview of products and scientific results*, A&A **571**, A1 (2014), 1303.5062

Planck Collaboration I, *Planck 2015 results. I. Overview of products and scientific results*, A&A **594**, A1 (2016), 1502.01582

Planck Collaboration II, *Planck 2015 results. II. Low Frequency Instrument data processings*, A&A **594**, A2 (2016), 1502.01583

Planck Collaboration Int. XIX, *Planck intermediate results. XIX. An overview of the polarized thermal emission from Galactic dust*, A&A **576**, A104 (2015), 1405.0871

Planck Collaboration Int. XLVI, *Planck intermediate results. XLVI. Reduction of large-scale systematic effects in HFI polarization maps and estimation of the reionization optical depth*, *ArXiv e-prints* (2016), 1605.02985

Planck Collaboration Int. XLVII, *Planck intermediate results. XLVII. Planck constraints on reionization history*, *ArXiv e-prints* (2016), 1605.03507

Planck Collaboration Int. XV, *Planck intermediate results. XV. A study of anomalous microwave emission in Galactic clouds*, A&A **565**, A103 (2014), 1309.1357

Planck Collaboration Int. XXII, *Planck intermediate results. XXII. Frequency dependence of thermal emission from Galactic dust in intensity and polarization*, A&A **576**, A107 (2015), 1405.0874

Planck Collaboration Int. XXX, *Planck intermediate results. XXX. The angular power spectrum of polarized dust emission at intermediate and high Galactic latitudes*, A&A **586**, A133 (2016), 1409.5738

Planck Collaboration IX, *Planck 2015 results. IX. Diffuse component separation: CMB maps*, A&A **594**, A9 (2016), 1502.05956

Planck Collaboration VIII, *Planck 2013 results. VIII. HFI photometric calibration and mapmaking*, A&A **571**, A8 (2014), 1303.5069

Planck Collaboration VIII, *Planck 2015 results. VIII. High Frequency Instrument data processing: Calibration and maps*, A&A **594**, A8 (2016), 1502.01587

Planck Collaboration X, *Planck 2015 results. X. Diffuse component separation: Foreground maps*, A&A **594**, A10 (2016), 1502.01588

Planck Collaboration XI, *Planck 2015 results. XI. CMB power spectra, likelihoods, and robustness of parameters*, A&A **594**, A11 (2016), 1507.02704

Planck Collaboration XII, *Planck 2013 results. XII. Diffuse component separation*, A&A **571**, A12 (2014), 1303.5072

Planck Collaboration XIII, *Planck 2015 results. XIII. Cosmological parameters*, A&A **594**, A13 (2016), 1502.01589

Planck Collaboration XV, *Planck 2013 results. XV. CMB power spectra and likelihood*, A&A **571**, A15 (2014), 1303.5075

Planck Collaboration XV, *Planck 2015 results. XV. Gravitational lensing*, A&A **594**, A15 (2016), 1502.01591

Planck Collaboration XVI, *Planck 2013 results. XVI. Cosmological parameters*, A&A **571**, A16 (2014), 1303.5076

Planck Collaboration XX, *Planck early results. XX. New light on anomalous microwave emission from spinning dust grains*, A&A **536**, A20 (2011), 1101.2031

Planck Collaboration XXI, *Planck early results. XXI. Properties of the interstellar medium in the Galactic plane*, A&A **536**, A21 (2011), 1101.2032

Planck Collaboration XXV, *Planck 2015 results. XXV. Diffuse low-frequency Galactic foregrounds*, A&A **594**, A25 (2016), 1506.06660

Planck Collaboration XXVI, *Planck 2015 results. XXVI. The Second Planck Catalogue of Compact Sources*, A&A **594**, A26 (2016), 1507.02058

Planck Collaboration XXVII, *Planck 2015 results. XXVII. The second Planck catalogue of Sunyaev-Zeldovich sources*, A&A **594**, A27 (2016), 1502.01598

Planck HFI Core Team, *Planck early results. VI. The High Frequency Instrument data processing*, A&A **536**, A6 (2011), 1101.2048

Robertson, B. E., Ellis, R. S., Furlanetto, S. R., Dunlop, J. S., *Cosmic Reionization and Early Star-forming Galaxies: A Joint Analysis of New Constraints from Planck and the Hubble Space Telescope*, ApJ **802**, L19 (2015), 1502.02024

Sazonov, S. Y., Sunyaev, R. A., *Microwave polarization in the direction of galaxy clusters induced by the CMB quadrupole anisotropy*, MNRAS **310**, 765 (1999), astro-ph/9903287

Seljak, U., Pen, U.-L., Turok, N., *Polarization of the Microwave Background in Defect Models*, *Physical Review Letters* **79**, 1615 (1997), astro-ph/9704231

Smith, K. M., et al., *Gravitational Lensing*, in S. Dodelson, D. Baumann, A. Cooray, J. Dunkley, A. Fraisse, M. G. Jackson, A. Kogut, L. Krauss, M. Zaldarriaga, K. Smith (eds.) American Institute of Physics Conference Series, *American Institute of Physics Conference Series*, volume 1141, 121–178 (2009), 0811.3916

Smoot, G. F., et al., *Structure in the COBE differential microwave radiometer first-year maps*, ApJ **396**, L1 (1992)

Sunyaev, R. A., Zeldovich, Y. B., *The Observations of Relic Radiation as a Test of the Nature of X-Ray Radiation from the Clusters of Galaxies*, *Comments on Astrophysics and Space Physics* **4**, 173 (1972)

Tucci, M., Toffolatti, L., *The Impact of Polarized Extragalactic Radio Sources on the Detection of CMB Anisotropies in Polarization*, *Advances in Astronomy* **2012**, 624987 (2012), 1204.0427

van Engelen, A., et al., *The Atacama Cosmology Telescope: Lensing of CMB Temperature and Polarization Derived from Cosmic Infrared Background Cross-correlation*, ApJ **808**, 7 (2015), 1412.0626

Willott, C. J., et al., *Eddington-limited Accretion and the Black Hole Mass Function at Redshift 6*, AJ **140**, 546 (2010), 1006.1342

Zaldarriaga, M., Seljak, U., *All-sky analysis of polarization in the microwave background*, Phys. Rev. D **55**, 1830 (1997), astro-ph/9609170

Zaldarriaga, M., Spergel, D. N., Seljak, U., *Microwave Background Constraints on Cosmological Parameters*, ApJ **488**, 1 (1997), astro-ph/9702157

Zeldovich, Y. B., Sunyaev, R. A., *The angular distribution of the microwave background, and its intensity in the direction of galaxy clusters*, *Soviet Astronomy Letters* **6**, 285 (1980)